A modified cohesive zone model for fatigue delamination in adhesive joints: numerical and experimental investigations

Ahmad S.M. Al-Azzawi [a,c,*] , L.F. Kawashita [b], C.A. Featherston [a]

[a] *School of Engineering, Cardiff University, The Parade, Cardiff, CF24 3AA, UK.*

[b] *Bristol Composites Institute, University of Bristol, University Walk, Bristol, BS8 1TR, UK.*

[c] *College of Engineering, University of Babylon, Babylon, Iraq.*

Abstract

A modified cohesive zone model (CZM) has been developed to simulate damage initiation and evolution in Fibre-Metal Laminates (FMLs) manufactured in-house but based on the Glare® material specifications. Specimens containing both splice and doubler features under high cycle fatigue loading. The model uses a novel trapezoidal traction-separation law to describe the elastic-plastic behaviour of this material under monotonic and high-cycle fatigue loading. The model is implemented in the software Abaqus/Explicit via an user-defined cohesive material subroutine. Several models of increasing complexity were investigated to validate the proposed approach. A two-stage experimental testing programme was then conducted to validate the numerical analyses. Firstly, quasi-static tests were used to determine the ultimate tensile strength (UTS) of a series of specimens with and without internal features. Secondly, high-cycle fatigue tests were conducted on both laminate types with variable load amplitude so that S-N curves could be built. Tests were monitored using digital image correlation (DIC) for full-field strain mapping and acoustic emission (AE) sensing to detect the initiation and propagation of damage during quasi-static and fatigue tests. Good correlation was observed between predicted onset and growth of delaminations and the history of cumulative AE energy during the tests, which supports the validity of the cohesive modelling approach for FMLs.

Keywords: Fibre Metal Laminates (FMLs), Glare®, Fatigue, Delamination, Cohesive Zone Model (CZM), Digital Image Correlation (DIC) and Acoustic Emission (AE).

* Corresponding author. Email address: ahmadsaddy@yahoo.com

1 Introduction

Fibre-metal laminates (FMLs) like Glare® are manufactured from metal sheets bonded with glass fibre reinforced composites using high toughness thermoset matrix materials. Where large panels are required, joints including splices (staggered overlapping layers) and doublers (additional external or internal layers) are used. One of the most common failure modes for FML structures is delamination in these joints [1]. Delamination in fibre composites has been modelled by researchers using a number of different approaches. These include the cohesive zone model (CZM) which incorporates both continuum damage and fracture mechanics concepts [2] and which has been used to model delamination initiation and propagation under high cycle fatigue [3-7]. This paper describes work done to extend the CZM approach to model elastic-plastic behaviour such as that exhibited in FMLs.

Fatigue has been shown to account for at least 90% of all service failures due to mechanical faults across a range of industries [8]. With the increased use of hybrid materials such as Glare® in aircraft and other critical structures it is important to be able to predict fatigue damage behaviour in these more complex materials and particularly in associated manufacturing features such as splices and doublers. This can be achieved by both experimental and analytical methods. Experimental studies usually focus on mechanical characterisation through tension-tension cyclic loading tests, yielding either S-N curves for fatigue life estimation or Paris-type curves for crack growth rate estimation. Analytical techniques provide efficient design and analysis methods which are particularly important for industrial applications. A number of studies have been conducted into modelling damage in the adhesive joints of composite laminates under fatigue loads. Models are generally based on either stress or strain analysis. Adhesive damage models reported in the literature use a number approaches including fracture mechanics and continuum damage mechanics [9-12]. In such approaches a damage parameter (D) is defined which modifies the constitutive response of the adhesive, with damage accumulation expressed in terms of the number of cycles to failure. However, although continuum damage approaches provide a valuable predictive framework, they do not give a clear definition of the fatigue initiation and propagation phases.

Nowadays, nonlinear Finite Element (FE) simulations including cohesive zone models (CZM) are widely used in modelling damage in fibre composites and FML joints. These models are based on both continuum damage mechanics and fracture mechanics concepts. The CZM was originally introduced by Barenblatt [13] based on Griffith's theory of fracture. Hillerborg *et al.* [14] implemented CZM in the framework of the FE method. Contrary to previous works, where the cohesive zone tractions had been defined as a function of the distance to the crack tip, they defined tractions versus crack opening displacement and the prevailing CZM traction–separation law was formed. Other

researchers including Needleman [15] and Tvergaard [16] extended the model by proposing various traction–separation functions and applying it to different problems. The fundamental concept however remained essentially unchanged. The cohesive zone model has since been employed by numerous authors for predicting the fatigue response of structures, coupling the CZM with fatigue damage evolution laws to simulate fatigue degradation. A number of authors [17-21] modelled fatigue loading cycle by cycle, which is computationally expensive and impractical in the case of high cycle fatigue. Others have tried to reduce the computational effort by the employment of cyclic extrapolation techniques [3, 22]. May and Hallett [23] first developed a cohesive law that combines phenomenological S-N curves for damage initiation with a fracture and damage mechanics approach for crack propagation for the simulation of damage under cyclic loading. This model was further developed by Harper and Hallett [6] for modelling delamination crack propagation in composite laminates under cyclic loading. The methodology has been further developed and expanded for the analysis of delamination propagation in composites under mixed-mode high-cycle fatigue loading [4, 7, 24].

Little work has been done however to examine the initiation and propagation of damage in the adhesive joints of fibre metal laminates under high cycle fatigue. Crocombe and Sugiman [25] conducted experimental and numerical investigations on metal laminate (ML) and Glare® laminates with doublers under fatigue tension loading, using the cohesive zone model proposed by Khoramishad *et al.* [24] for the simulation of damage evolution at interfaces. More recently Hosseini-Mazaheri and Toudeshky [26] developed an elastic–plastic-damage constitutive law to simulate delamination initiation and propagation in FMLs; however this model was limited to a low-cycle fatigue loading regime.

This study concentrates on modelling damage in Glare® laminate joints (both splices and doublers) under high cycle fatigue loading. This is achieved by applying a trapezoidal traction law for the cohesive layers at the metal-fibre interfaces which is more representative of high toughness adhesive interfaces. A modified cohesive zone model using this mixed mode traction law is developed and implemented through a user-defined VUMAT subroutine in the Abaqus/Explicit software, to model the onset and growth of delamination in the aluminium-composite interfaces. Experimental tests on Glare® laminates containing either splice or doubler features are then used to validate the model.

2 Cohesive Zone Model (CZM)

Cohesive zone models have been widely used for predicting delamination in adhesively bonded structures under fatigue loading. Models used in these analyses which are mostly based on a bi-

linear traction-separation law have been found to be a particularly efficient approach for elastic materials. The same approach however has not been found to be accurate for elastic-plastic materials where a trapezoidal traction-separation law has proved to be more efficient in predicting the plastic flow of ductile adhesives [27].

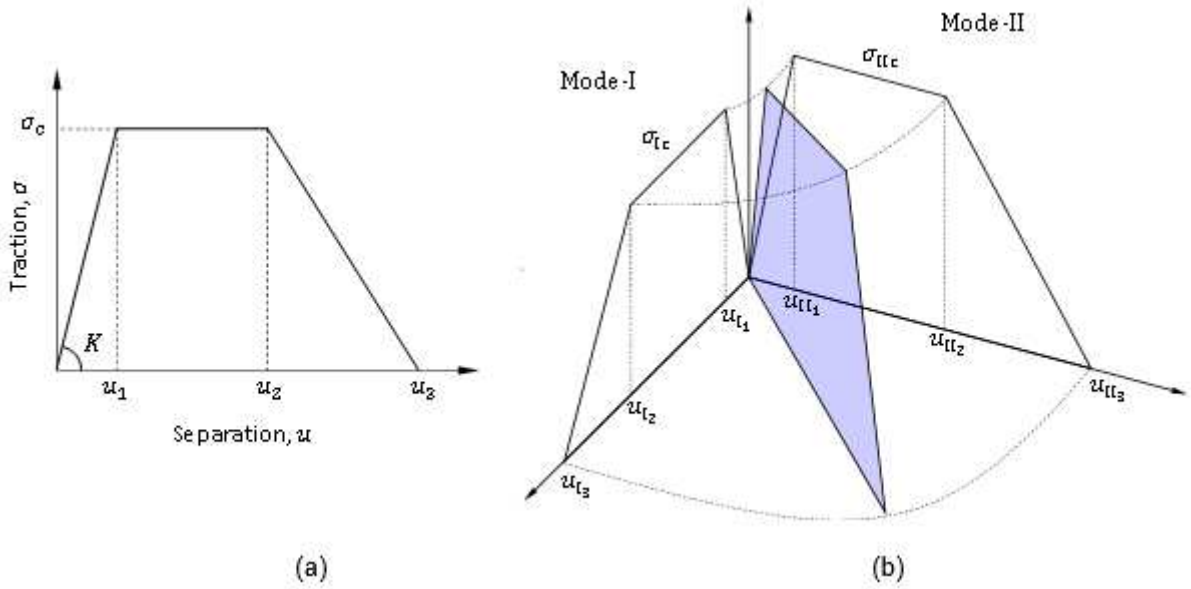

Figure 1: Mixed mode trapezoidal traction law; u_1 and u_2 are the separations at the end of the elastic and plastic (constant-stress) regions respectively, u_3 are the separations at failure, and σ_c are the constant stresses. The subscripts I and II represent mode-I and mode-II respectively.

The trapezoidal traction law shown in Figure 1(a) has been adopted by many researchers [16, 28-35] to model interface damage behaviour in elastic or elastic-plastic materials in either mode-I or mode-II under static loading. In this work, a mixed mode trapezoidal traction-separation law has been developed (Figure 1 (b)) to model first static and then high cycle fatigue damage in FML structures including adhesively bonded joints. Deterioration due to the influence of fatigue loading is simulated by degrading the trapezoidal traction-separation response based on a fatigue damage variable derived from the Paris law for the material and the elapsed number of load cycles. This trapezoidal traction separation law has been implemented in Abaqus/Explicit using 2D cohesive elements which have been utilised in a two-stage fatigue loading analysis as shown Figure 2.

In the first step static loading up to the maximum fatigue load value is applied after which the second step including the loading envelope approach shown in Figure 2 (a) begins. This process requires the use of two algorithms to simulate both quasi-static and high cycle fatigue damage behaviour, following the trapezoidal traction law and the fatigue Paris law respectively. This fatigue degradation process is illustrated in Figure 2 (b) and is based on a total damage variable which is the sum of both static and fatigue damage variables. This fatigue damage variable (D_{f}) is zero at the end of the static step and is then updated according to the Paris law for each increment. During analysis, it increases

up to certain value D_{f,t_1} at simulation time t_1 which indicates the start of the loading envelope-based fatigue degradation. Fatigue damage then continues to evolve following the trapezoidal traction law up to damage variable D_{f,t_2} at simulation time t_2 at the beginning of the softening region. The process continues until final fatigue failure occurs, when $D_{\mathrm{f}} = 1$ and the simulation time indicates the number of elapsed fatigue cycles.

A detailed explanation of the static and fatigue cohesive models is provided below, with a flowchart summarising the implementation being provided later (Figure 5).

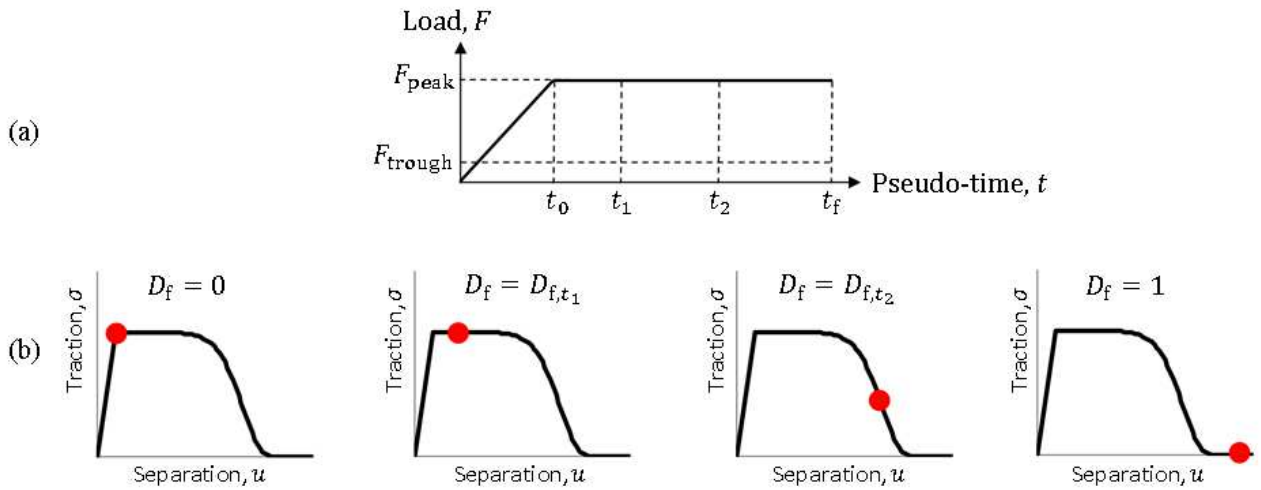

Figure 2: Fatigue load envelope (a) and fatigue degradation of the cohesive zone (b).

2.1 Quasi-static damage model

The first stage in this process was to create a static damage model based on the trapezoidal traction-separation law shown in Figure 1. This was done by writing a user-defined material subroutine which was then built into the software Abaqus/Explicit. The VUMAT interface provides the displacement jump at each cohesive integration point and requires the user subroutine to return the resulting traction vector, with the ability to store and update a number of extra state variables (SDVs). The subroutine developed here decomposed the displacement jump increments into mode-I (u_{I}) and mode-II (u_{II}) components, which were then used to update the normal stresses σ_{I} and shear stresses σ_{II} at each cohesive integration point. These displacements are then used to calculate the damage initiation index, D_{init}, which predicts initiation based on a quadratic stress criterion [36], *i.e.*

$$\left(\frac{\sigma_{\mathrm{I}}}{\sigma_{\mathrm{IC}}}\right)^2 + \left(\frac{\sigma_{\mathrm{II}}}{\sigma_{\mathrm{IIC}}}\right)^2 = D_{\mathrm{init}} \tag{1}$$

Strain energy release rates (SERRs) G_{I} and G_{II} are then calculated from the areas under the

trapezoidal traction-separation curves for mode-I and mode-II, namely

$$G_{\mathrm{I}} = \int_0^{u_{\mathrm{I}}} \sigma_{\mathrm{I}} \, \mathrm{d}u_{\mathrm{I}} \ , \tag{2}$$

$$G_{\mathrm{II}} = \int_0^{u_{\mathrm{II}}} \sigma_{\mathrm{II}} \, \mathrm{d}u_{\mathrm{II}} \ . \tag{3}$$

Finally, the damage evolution variable D_{e} is calculated using a power law failure criterion,

$$\left(\frac{G_{\mathrm{I}}}{G_{\mathrm{IC}}}\right)^{\phi} + \left(\frac{G_{\mathrm{II}}}{G_{\mathrm{IIC}}}\right)^{\phi} = D_{\mathrm{e}} \ , \tag{4}$$

where the power law parameter ϕ must be determined from a best fit to mixed-mode delamination data from the literature [37,38]. The strain energy release rate for the interface between aluminium 2024-T3 and FM94 reinforced with S2 glass fibre used here is based on experiments performed by Vesco *et al.* [39]. An important aspect of the mixed mode case is the lower total critical energy release rate G_{C} compared to pure mode-I and mode-II situations. Neither the Benzeggagh-Kenane criterion described in [3], nor the power law criterion with $\phi \geq 1$ can correctly describe the delamination behaviour of Glare®. A better relationship for this specific case is the power law with $\phi = \frac{1}{2}$ [38].

2.2 Fatigue damage model

A fatigue damage degradation law was then developed for this trapezoidal traction-separation law. The fatigue damage approach adopted in this model to calculate crack growth rate is a normalised Paris law according to [3, 5-7],

$$\frac{\mathrm{d}a}{\mathrm{d}N} = C\left(\frac{\Delta G}{G_{\mathrm{C}}}\right)^{m} , \tag{5}$$

where $\mathrm{d}a/\mathrm{d}N$ is the crack growth rate (the increment in crack length with increasing number of cycles) while C and m are best fit coefficients to experimental data in a log-log plot for crack length a versus number of cycles N. The total critical strain energy G_{C} is a material property for the interface cohesive layer (whose value has been adapted from [40]) and represents the area under the curve of the trapezoidal traction–separation relation which in this study is for pure mode-II – the predominant failure mechanism for both splice and doubler specimens according to previous work by the authors [41, 42].

The mode-II strain energy release rate *amplitude* is calculated as in [39, 40],

$$\Delta G = (1 - R^2)\, G_{\max} \ , \tag{6}$$

where R is the load ratio (trough load divided by peak load), which in this study is equal to 0.1, and $G_{\max}$ is the peak strain energy release rate.

The fatigue damage variable D_{f} is calculated based on an effective length $\bar{L}$ which is associated with a single cohesive integration point in the direction of crack propagation. The delamination will propagate this distance $\bar{L}$ when this cohesive integration point fails, which will happen after a given number of cycles has elapsed, *i.e.*

$$N_{\mathrm{f}} = \bar{L} \cdot \left(\frac{\mathrm{d}a}{\mathrm{d}N}\right)^{-1}, \tag{7}$$

where $\mathrm{d}a/\mathrm{d}N$ is the crack growth rate obtained from the modified Paris law, equation (5). We define the time of failure for the cohesive integration point as,

$$t_{\mathrm{f}} = N_{\mathrm{f}} \cdot \omega^{-1}, \tag{8}$$

where ω is the user-defined loading frequency in cycles per unit pseudo-time. The damage accumulated during the current time step Δt is therefore,

$$\Delta D = \Delta t \cdot (t_{\mathrm{f}})^{-1}. \tag{9}$$

Finally, this damage increment updates the fatigue damage variable for the next time step [6, 7, 43], *i.e.*

$${}^{t+\Delta t}D_{\mathrm{f}} = \ {}^{t}D_{\mathrm{f}} + \Delta D \ . \tag{10}$$

2.3 Unloading – reloading

To account for the partial unloading and reloading which may occur during crack propagation, the unloading and reloading paths need to be defined in the cohesive zone model. When the separation of the corresponding cohesive surfaces is smaller than in the previous time step, the unloading path is followed. In this research, unloading is prescribed to be directed back to the origin of the traction-separation curve [37] as shown in Figure 3. The traction components during unloading are then calculated algorithmically as follows.

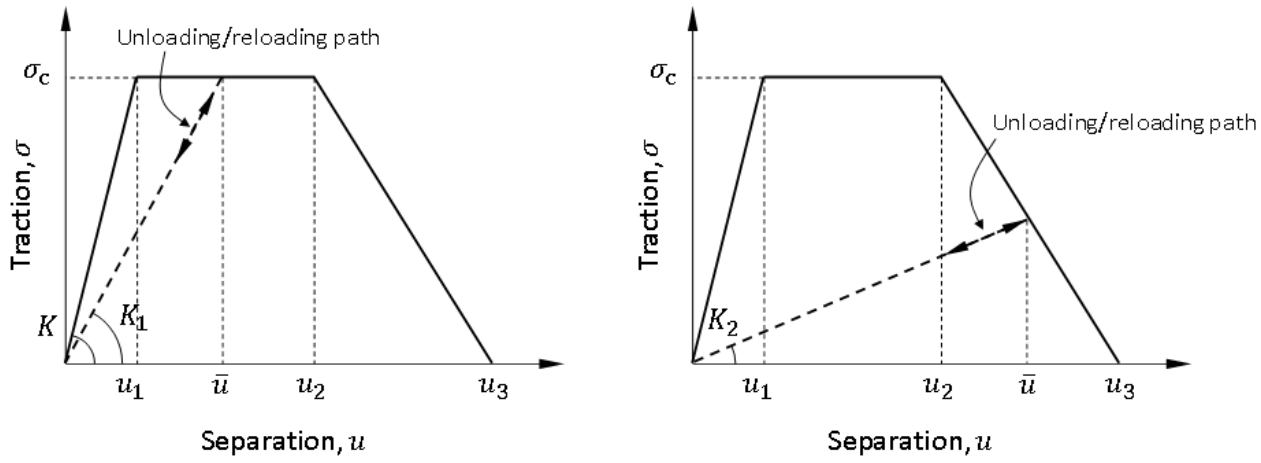

Figure 3: Unloading/reloading path for mixed mode trapezoidal traction law for (a) the constant stress-region and (b) the softening region.

Constant stress-region, Figure 3 (a):

If $u \geq \bar{u}$ (*i.e.* 'loading')

$$\sigma = \sigma_c \tag{11}$$

Else if $u < \bar{u}$ (*i.e.* 'unloading')

$$K_1 = \frac{\sigma_c}{\bar{u}} \tag{12}$$

$$\sigma = K_1 \cdot u \tag{13}$$

Linear softening region, Figure 3 (b):

If $u \geq \bar{u}$ (*i.e.* 'loading')

$$\sigma = \sigma_c \cdot \frac{u_3 - u}{u_3 - u_2} \tag{14}$$

Else if $u < \bar{u}$ (*i.e.* 'unloading')

$$\bar{\sigma} = \sigma_c \cdot \frac{u_3 - \bar{u}}{u_3 - u_2} \tag{15}$$

$$K_2 = \frac{\bar{\sigma}}{\bar{u}} \tag{16}$$

$$\sigma = K_2 \cdot u \tag{17}$$

where u is the is the displacement jump at the current increment, $\bar{u}$ is the local maximum displacement jump (*i.e.* the 'envelope' value of u), σ_c is the 'plateau' (*i.e.* constant) value of the cohesive traction, σ is the stress at the current time step, u_1, u_2, and u_3 are characteristic displacements of the trapezoidal law, and K_1 and K_2 are cohesive stiffnesses for the constant stress and the linear softening regions of the trapezoidal law, respectively.

2.4 Model implementation

The two-dimensional cohesive elements in Abaqus (COH2D4) have two integration points as shown in Figure 4. In order to provide a conservative criterion for cohesive element failure and subsequent removal from the analysis, the VUMAT subroutine requests the deletion of the element once *either* of the two integration points is completely degraded. Once this happens all element stresses and strains are set to zero and the deletion flag is activated; the solver then removes the failed element from the simulation in the following time step [44].

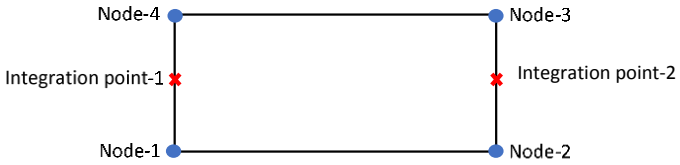

Figure 4: Schematic of a two-dimensional cohesive element (COH2D4).

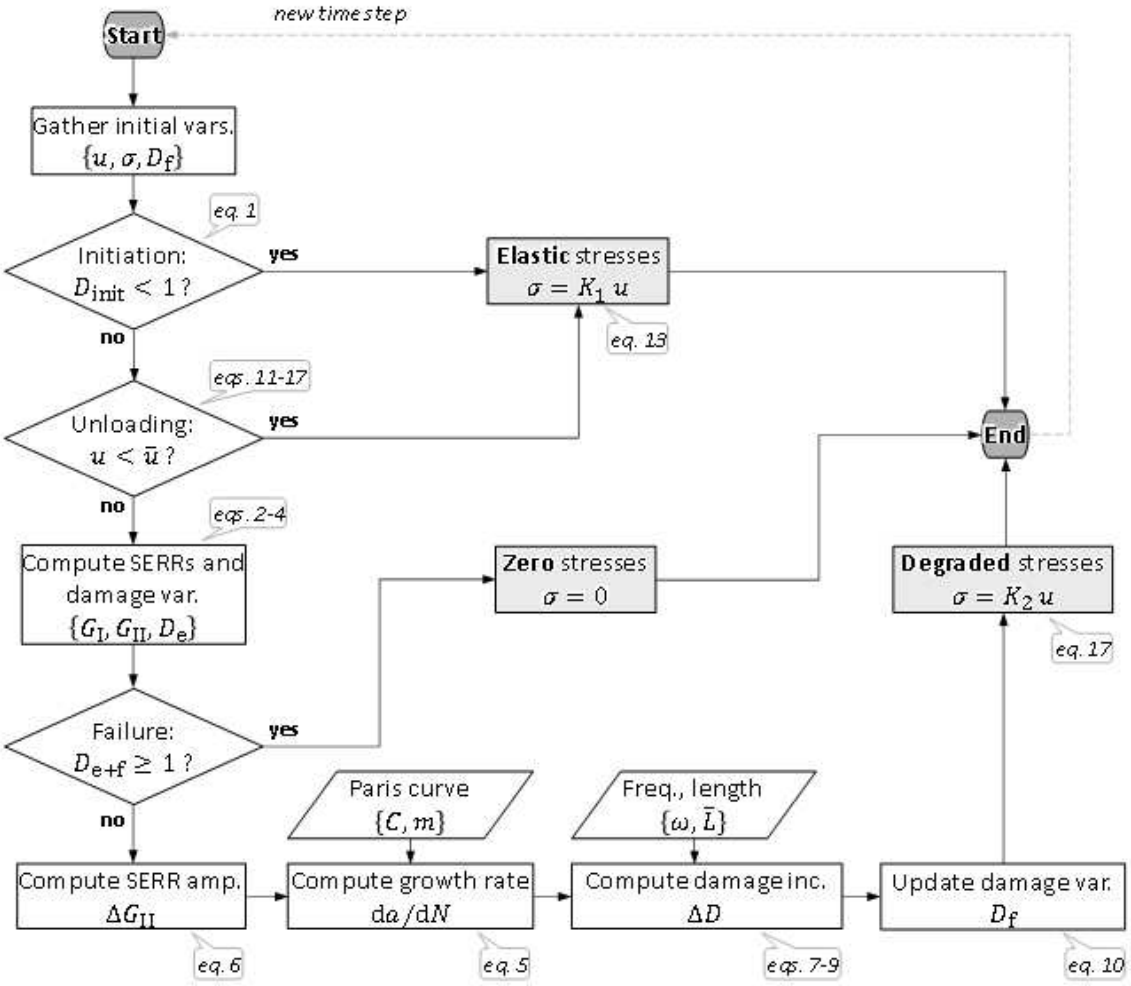

Figure 5: Flowchart describing the VUMAT implementation.

The VUMAT subroutine is called at each time increment for each cohesive integration point in the

model. The cohesive traction update scheme is shown in the form of a flowchart in Figure 5, which also indicates the sequence in which the various equations described above are evaluated.

2.5 Model verification

The proposed mode-II fatigue damage model was verified through the analysis of specimens containing a discontinuous (*i.e.* 'cut') central layer as shown in Figure 6. The FE model represents only a quarter of the specimen due to symmetries. The central aluminium layer was 0.1 mm thick while the two neighbouring aluminium layers were 0.4 mm thick. Each layer comprised 200 elements 0.25 mm long and was one element thick. The elements used were linear two-dimensional plane strain continuum elements (CPE4). The interfaces were meshed using the 2D cohesive elements described above (COH2D4) with an arbitrary '*geometrical thickness*' of 0.01 mm (the '*constitutive thickness*' is unity as usual). The model had an x-direction symmetry boundary condition applied to the left hand-side edge nodes of the continuous layers only. The properties of the aluminium and cohesive materials used in this model are given in Tables 1-5. RHS edge elements were subjected to prescribed horizontal displacements in quasi-static simulations, and prescribed loads in fatigue simulations (according to the envelope approach described earlier).

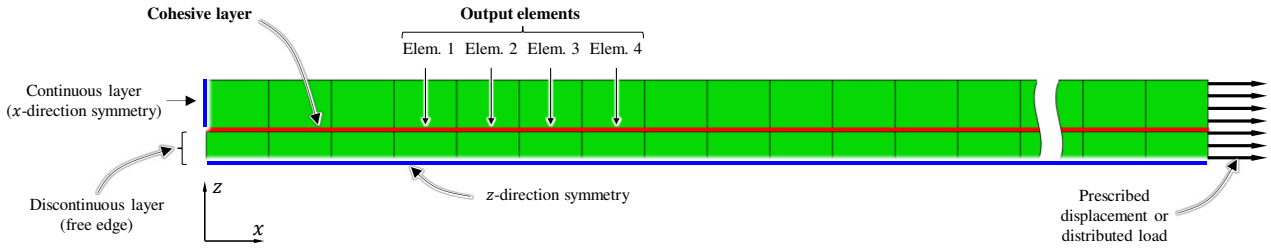

Figure 6: Quarter-model of the cut-ply specimen, showing planes of symmetry and four cohesive elements selected (arbitrarily) for detailed data output.

2.5.1 Quasi-static loading

The traction-separation curves for the cut ply model resulting from the VUMAT code proposed here are shown in Figure 7. A good representation of the trapezoidal traction law reported by Hutchinson [16] is achieved, as expected. The mode-II cohesive stiffness of 8.32×10^4 N/mm^3 and the shear 'yield stress' of 40 MPa are reproduced exactly, with damage initiation and linear softening occurring at a displacement jumps of 0.49 µm and 15.18 µm respectively, which agree with the input data provided.

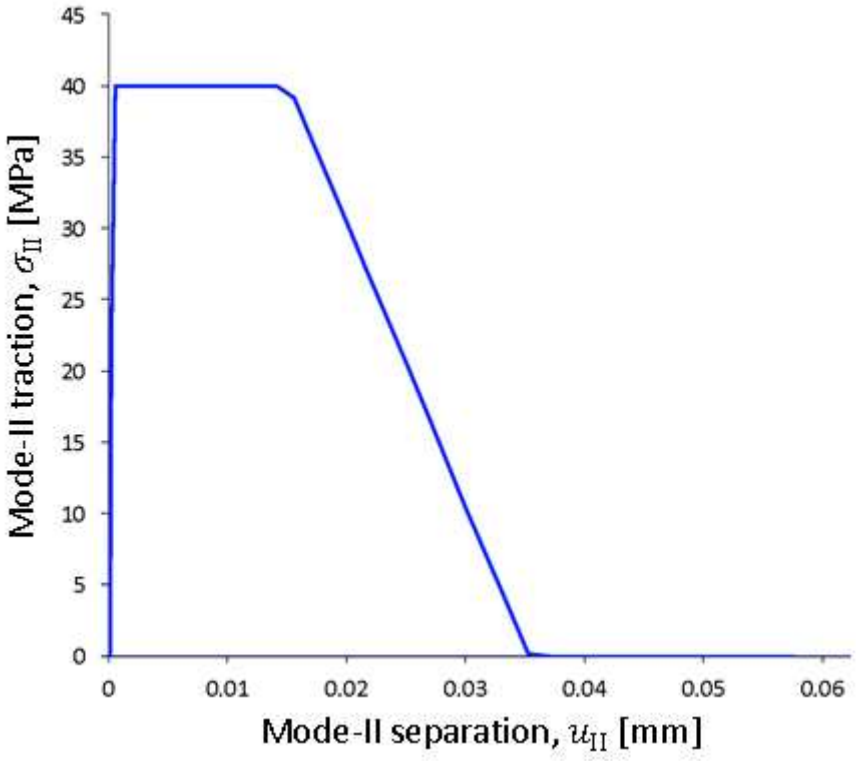

Figure 7: Traction-separation curve for 'output element 1' in the simplified cut ply model under quasi-static loading.

2.5.2 Fatigue loading

The traction-separation curves for the cut ply model under fatigue (70% load severity, R-ratio of 0.1) are shown in Figure 8. These prove that both static and fatigue curves are identical in the elastic region and the initial part of the constant stress region before fatigue damage is incurred. After this fatigue damage initiates (user-defined start time of 0.3 ms) leading to fatigue degradation in four 'sample' elements ahead of the numerical crack tip, confirming stable fatigue delamination growth due to the near-constant strain energy release rates observed in cut ply tests [7].

In order to validate the fatigue parameters used which were taken from experimental data reported by Alderliesten [45], the response for different fatigue load severities was predicted using the VUMAT code as shown in Figure 9. For clarity results for only four cohesive elements out of the 200 elements modelled are shown for four different severities (70%, 60%, 50% and 40%) which are compared with experimental Paris law results. The normalised mode-II strain energy release rate amplitudes $\Delta G_{\mathrm{II}}/G_{\mathrm{IIC}}$ are plotted against crack growth rates $\mathrm{d}a/\mathrm{d}N$, showing excellent correlation between predicted and experimental results.

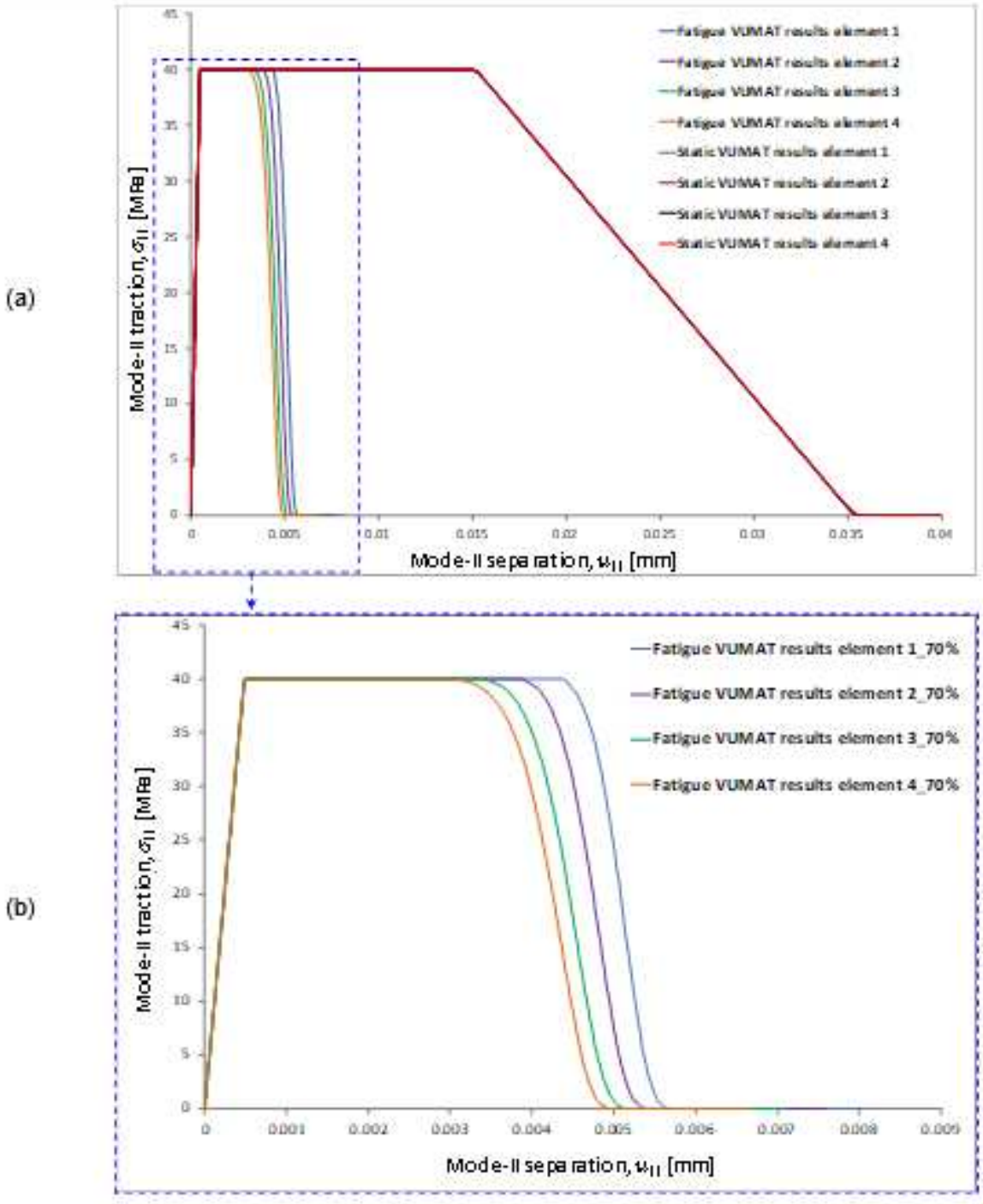

Figure 8: Traction-separation curves for the cut ply model under fatigue loading (70% severity); (a) comparison of fatigue and static traction separation curves, and (b) detail of the fatigue curves for four output elements.

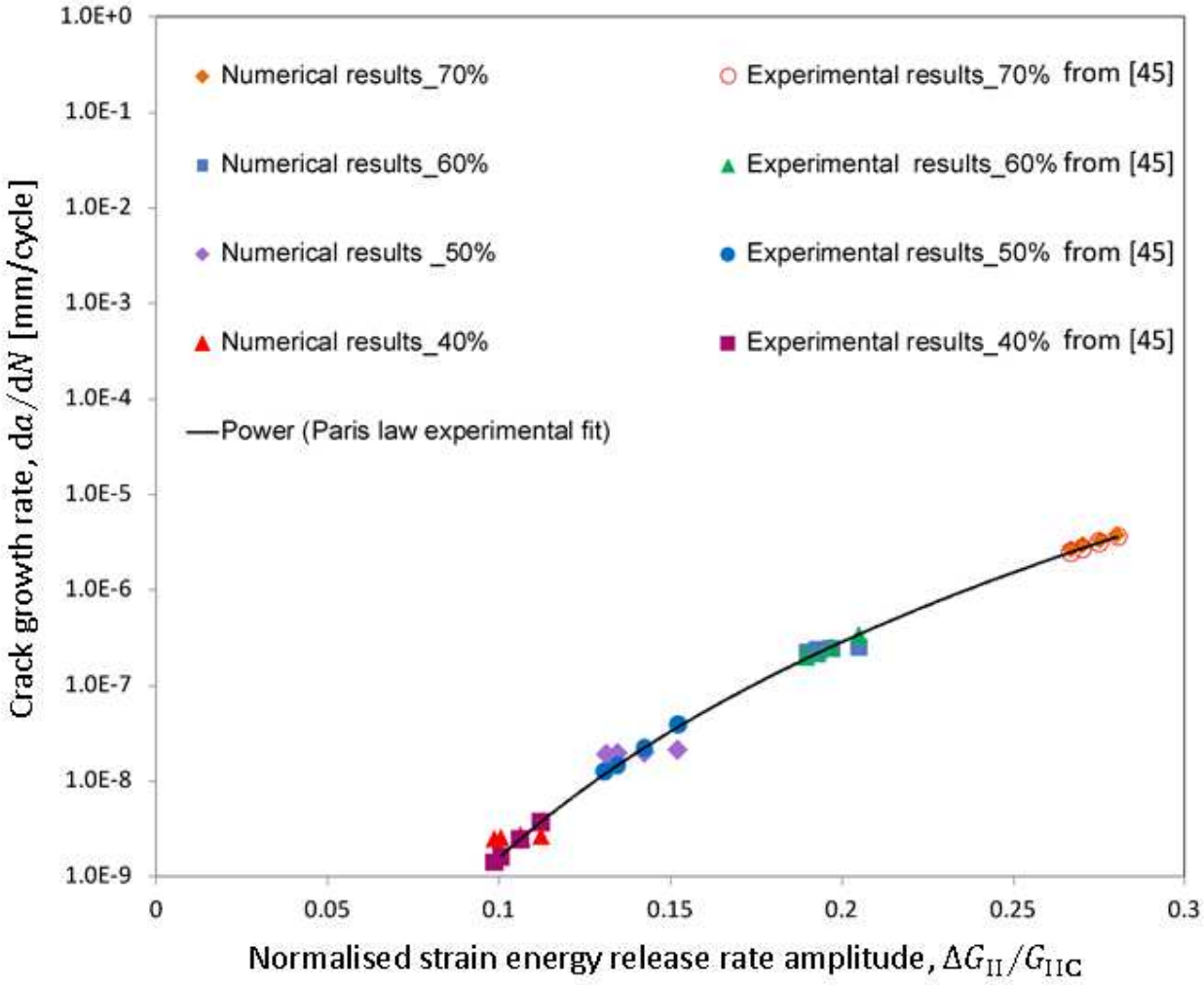

Figure 9: Experimental [45] and numerical Paris curves for the cut ply model under $R = 0.1$ and severities of 70%, 60%, 50% and 40%, as computed by the four output cohesive elements.

3 Fatigue of doubler and splice joints

3.1 Specimen design

The joints examined were longitudinal splice and transverse doubler joints manufactured in-house but based on the Glare®4B specification as shown in Figure 10. The specimens had a gauge section measuring 153 mm × 13.5 mm and two 53 mm long aluminium tabs bonded on each end. These were manufactured from 0.4 mm thick sheets of aluminium alloy 2024-T3 and Cytec™ S2-glass/FM94 glass fibre reinforced polymer (GFRP) unidirectional prepreg. The layups were designed according to the specification for commercial Glare® 4B shown in Table 1 [1].

The manufacturing process involved first etching the aluminium sheets to remove the oxide layers. Mechanical abrasion using Scotch-Brite™ abrasive sponges was followed by degreasing using Methyl Ethyl Ketone (MEK). The sheets were then immersed in a solution of 100 g/L of water of sodium hydroxide (NaOH), at 60 °C for 1 min and then a water solution of 330 mL/L chromic-sulphuric acid (97% v/v) and 50 g/L potassium dichromate at 60 °C for 15 min. After these latter two stages the sheets were rinsed in tap water for 20 minutes and then dried in an oven at 40 °C for 30 minutes.

Lay-up was carried out by hand and followed by autoclave curing. The cure cycle involved heating to 120 °C at a rate of (1.7 - 2.8 °C) min^{-1} under a pressure of 1.86 bar and with a vacuum of 0.9 bar applied, holding for 60 minutes and then cooling at a rate of 3 °C min^{-1}. Finally the specimens were cut to size using a spiral tooth carbide milling cutter at a cutting speed of 2000 – 3000 rpm and a feed rate of 500 mm/min.

As these laminates were manufactured in-house their mechanical properties are not guaranteed to meet the specification of commercial Glare®; however the authors have observed comparable properties between the two materials in previous work [41-43]. Each GFRP layer had three plies with the layup [90º/0º/90º] and a cured ply thickness of 0.133 mm. The layup on one side of the joint was '3/2' (three layers of aluminium and two layers of GFRP) and on the other '4/3' (four layers of aluminium and three layers of GFRP).

Table 1: Standard grades of commercial Glare® [1].

Grade	Sub-grade	Alloy	Metal sheet thickness [mm]	GFRP sub-laminate layup	Main beneficial characteristics
Glare® 1	-	7475-T761	0.3 – 0.4	0 / 0	fatigue, strength
Glare® 2	Glare® 2A	2024-T3	0.2 – 0.5	0 / 0	fatigue, strength
Glare® 2	Glare® 2B	2024-T3	0.2 – 0.5	90 / 90	fatigue, strength
Glare® 3	-	2024-T3	0.2 – 0.5	0 / 90	fatigue, impact
Glare® 4	Glare® 4A	2024-T3	0.2 – 0.5	0 / 90 / 0	fatigue, strength (especially in 0° direction)
Glare® 4	Glare® 4B	2024-T3	0.2 – 0.5	90 / 0 / 90	fatigue, strength (especially in 90° direction)
Glare® 5	-	2024-T3	0.2 – 0.5	0 / 90 / 90 / 0	impact
Glare® 6	Glare® 6A	2024-T3	0.2 – 0.5	+45 / -45	shear, off-axis properties
Glare® 6	Glare® 6B	2024-T3	0.2 – 0.5	-45 / +45	shear, off-axis properties

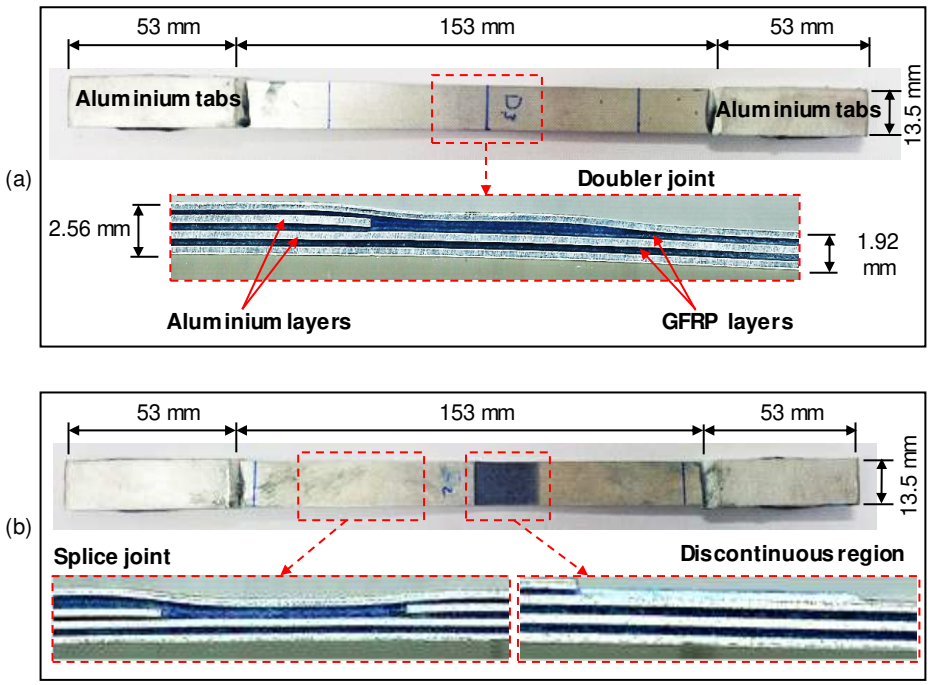

Figure 10: Specimen design for (a) doubler (b) splice (images resized for clarity, not to scale).

3.2 Finite element models

Two-dimensional FE models of the splice and doubler joints were created to simulate the effect of fatigue delamination in fibre metal laminate structures containing adhesive joints. This involved extracting the geometry and thickness of each layer from detailed scans of the actual specimens, as shown in Figure 10, and then meshing them using plane strain elements (CPE4), Figures 11 and 12. The interfaces were meshed using 2D cohesive elements (COH2D4). The geometry and thickness of each layer were extracted from detailed scans of real specimens and a high-fidelity structural mesh was generated to represent the observed internal geometry.

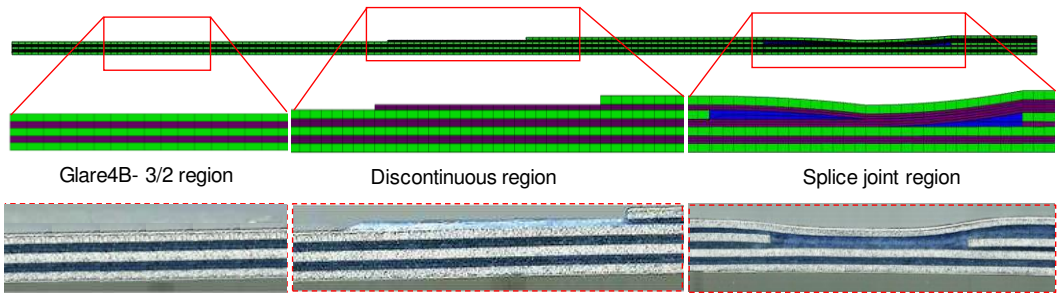

Figure 11: Finite element mesh of the splice specimen (top) based on optical scans of real specimens (bottom) (images resized for clarity, not to scale).

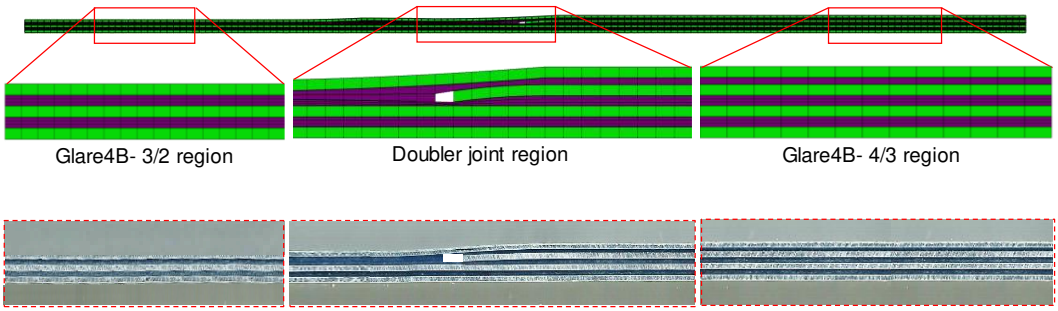

Figure 12: Finite element mesh of the doubler specimen (top) based on optical scans of real specimens (bottom) (images resized for clarity, not to scale).

A comprehensive literature review was carried out in order to gather reliable mechanical properties for the Glare® material constituents. The properties of aluminium, GFRP, bulk FM94 resin and cohesive layers used are presented in Tables 2-6. Mechanical properties for the S2-glass/FM94 GFRP material were given in [25] and are shown in Table 2. Properties for the aluminium alloy 2024-T3 were obtained from [45] and are summarised in Table 3. The cohesive properties for GFRP-metal interfaces were obtained from [46] and are shown in Table 4. The cohesive stiffnesses K_{I} and K_{II} were calculated based on the elastic properties of bulk FM94 resin, shown in Table 5, assuming that the interfacial stiffness is dominated by the deformation of a 10 µm thick resin rich layer, as described in [7] (it should be noted that these stiffnesses have only minor influence on the fracture initiation and propagation behaviour of the CZM, which instead is more strongly dependent on the initiation stresses, σ_{Ic} and σ_{IIc}, and the critical strain energy release rates, G_{IC} and G_{IIC}). The fracture process resulting from the delamination of the GFRP-metal interfaces is micro-mechanically different from the fracture process observed between the same metal and resin in the absence of fibres, since the presence of fibres precludes the development of a local plastic zone within the toughened epoxy material [47]. As a result, much higher fracture energies are expected within the resin pockets formed around the splice and doubler features contained in the laminates investigated here. Indeed, Katnam *et al.* [48] obtained the cohesive properties shown in Table 6 for fracture in a similar material system, but along a 100 µm thick unreinforced resin layer. The properties in Table 6 were therefore assumed for the interfaces formed around resin pockets in the splice and doubler features investigated here.

Table 2: Mechanical properties for S2-glass/FM94 prepreg material [25]

Property	**Value**	**Units**
Young's modulus, fibre direction, E_{11}	50.0	GPa
Young's modulus, transverse direction, E_{22}	9.0	GPa
Poisson's ratio, ν_{12}	0.33	-
Poisson's ratio, ν_{23}	0.04	-
In-plane shear modulus, G_{12}	3.5	GPa
Transverse shear modulus, G_{23}	3.0	GPa
Fibre-direction tensile strength, X_{T}	2000	MPa
Fibre-direction compressive strength, X_{C}	550	MPa
Transverse tensile strength, Y_{T}	43	MPa
Transverse compressive strength, Y_{C}	90	MPa
In-plane shear strength, S_{12}	93	MPa
Transverse shear strength, S_{23}	50	MPa
Critical SERR, fibre direction, $G_{\mathrm{C},X}$	12.0	kJ·m^{-2}
Critical SERR, transverse direction, $G_{\mathrm{C},Y}$	1.0	kJ·m^{-2}
Mass density, ρ [49]	2000	kg·m^{-3}
Coefficient of thermal expansion, fibre direction [45]	6.1×10^{-6}	ºC^{-1}
Coefficient of thermal expansion, transverse direction [45]	26.2×10^{-6}	ºC^{-1}

Table 3: Mechanical properties for aluminium alloy 2024-T3 [1].

Property	**Value**	**Units**
Young's modulus	72.4	GPa
Stress at 4.7% strain	420	MPa
Tensile yield strength, rolling direction	300	MPa
Tensile yield strength, transverse direction	299	MPa
Shear modulus	27.6	GPa
Poisson's ratio	0.33	-
Coefficient of thermal expansion	22×10^{-6}	ºC^{-1}
Mass density	2780	kg·m^{-3}

Table 4: Cohesive zone properties for GFRP-metal interfaces.

G_{IC} (kJ·m^{-2}) [46]	G_{IIC} (kJ·m^{-2}) [46]	σ_{Ic} (MPa) [46]	σ_{IIc} (MPa) [46]	K_I (N·mm^{-3})	K_{II} (N·mm^{-3})
0.45	1.0	40	40	2.189×10^{5}	0.823×10^{5}

Table 5: Mechanical properties for the FM94 resin [50].

Property	**Value**	**Units**
Young's modulus	2.19	GPa
Poisson's ratio	0.33	-
Mass density [50, 51]	1280	kg·m^{-3}
Coefficient of thermal expansion [51]	100×10^{-6}	ºC^{-1}

Table 6: Cohesive zone properties for bulk resin-metal interfaces.

G_{IC} (kJ·m^{-2}) [48]	G_{IIC} (kJ·m^{-2}) [48]	σ_{Ic} (MPa) [38]	σ_{IIc} (MPa) [38]	K_I (N·mm^{-3})	K_{II} (N·mm^{-3})
2.0	4.0	50	50	2.189×10^{5}	0.823×10^{5}

3.3 Test setup

A two-stage experimental testing programme was performed in order to support the numerical analyses. Firstly, quasi-static tests were used to obtain the ultimate tensile strength (UTS) of the manufactured specimens and hence determine appropriate values for the fatigue loading severities. Then, fatigue life curves were extracted for specimens containing both splice and doubler joints in order to study fatigue behaviour of FMLs including these features.

Prior to testing, doubler specimens were pre-loaded to generate a crack initiation site (this was not necessary for splice specimens in which cracks naturally grow from the discontinuity at the outer surface). This was achieved by loading the specimens slowly in tension whilst using a camera with a high magnification micro-lens as shown in Figure 13 to monitor crack initiation and propagation. When the crack length reached 1 mm the test was stopped.

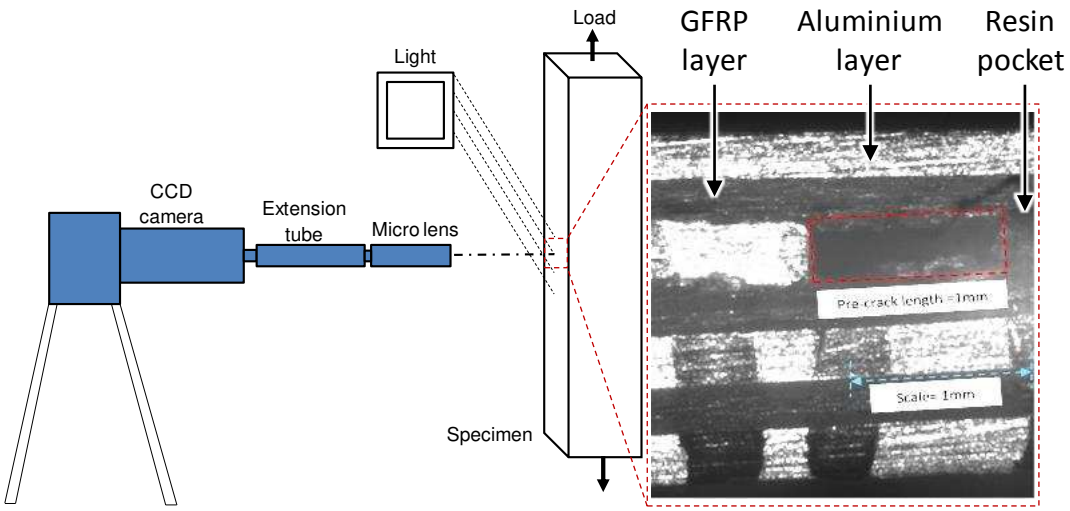

Figure 13: Micro-video camera setup for through-thickness crack measurement left and 2D micro-image for pre-cracked doubler specimen right.

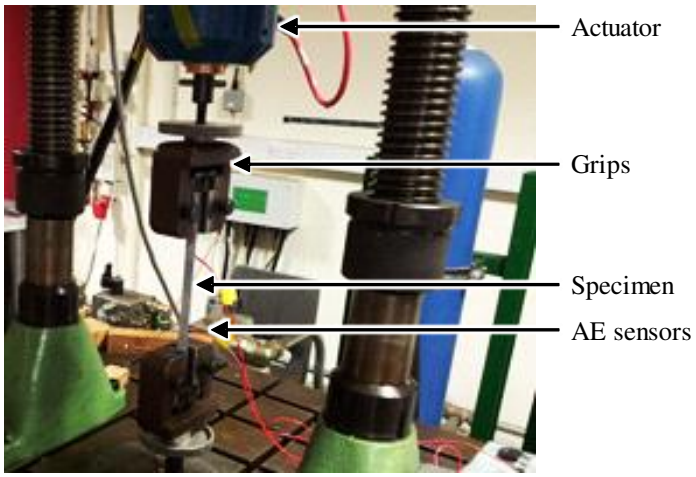

Figure 14: Experimental fatigue test setup.

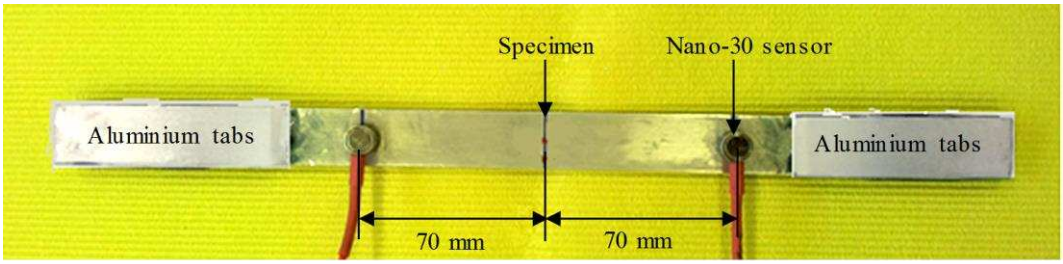

Figure 15: AE sensor's position on a Glare® 4B specimen.

Specimens were tested in an MTS servo-Hydraulic (50 kN) machine as shown in Figure 14 with a constant load ratio $R = 0.1$ and a frequency of 5 Hz. Different severities were investigated for both splice and doubler specimens based on maximum fatigue loads calculated from ultimate tensile strengths obtained from quasi-static tests on splice and doubler specimens and described in [52].

Two Acoustic Emission (AE) sensors were mounted on the specimens to monitor damage events during fatigue tests. These were Nano-30 sensors supplied by Mistras Group™ which have a mid-band frequency range of 125-750 kHz. These sensors were chosen because of their small size (8 mm diameter) which enabled them to be mounted on these relatively narrow specimens, and because they have a high resonant response up to 300 kHz making them suitable for monitoring the signals expected. They were bonded to the specimens using the multi-purpose silicone sealant *Loctite*™ 595 as shown in Figure 15. Each sensor was connected to a Mistras Group™ pre-amplifier with a 40 dB gain (just above the background noise level) to allow the signal to be translated along the required length of cable and low frequency filtering was applied using a band-pass filter of 20-1200 kHz to remove undesirable mechanical noise. The pre-amplifiers were in turn connected to a Mistras Group™ PCI2 acquisition unit. The detection settings were a 45 dB threshold and a sampling rate of 5 MHz.

4 Numerical results

The traction-separation curves for a series of five cohesive elements in the path of the fatigue crack growth in the splice specimen are shown in Figure 16 (b) (note that damage propagates from left to right, *i.e.* from element 1 towards element 5). It can be seen that for each element these curves follow the static softening curve for a considerable portion of the elastic region, up to the point where the elements become part of the numerical crack front and degrade rapidly due to fatigue damage. It should be noted that the computed strain energy release rate G_{II} increases with increasing crack length (since the areas under the traction-separation curves increase between elements 1 and 5) which suggests an acceleration in crack growth upon fatigue damage initiation. The evolution of the damage variable D_{tot} is illustrated in Figure 18 for the 50% severity case, where fringe colours vary continually from blue ($D_{\mathrm{tot}} = 0$) to red ($D_{\mathrm{tot}} = 1$) confirming the progressive nature of the traction-separation curves under fatigue.

In order to validate the numerical results, failure times from the VUMAT model were compared with experimental data obtained by Alderliesten [45] from fatigue tests on Glare® 2 and Glare® 4B specimens giving Paris Law coefficients $C = 0.005$ and $m = 0.75$. These coefficients were used to derive the continuous line in Figure 19 against which numerical results are compared. It can be seen that the numerical VUMAT subroutine results correlate well with the experimental results, for all five 'sample' elements and all severity levels.

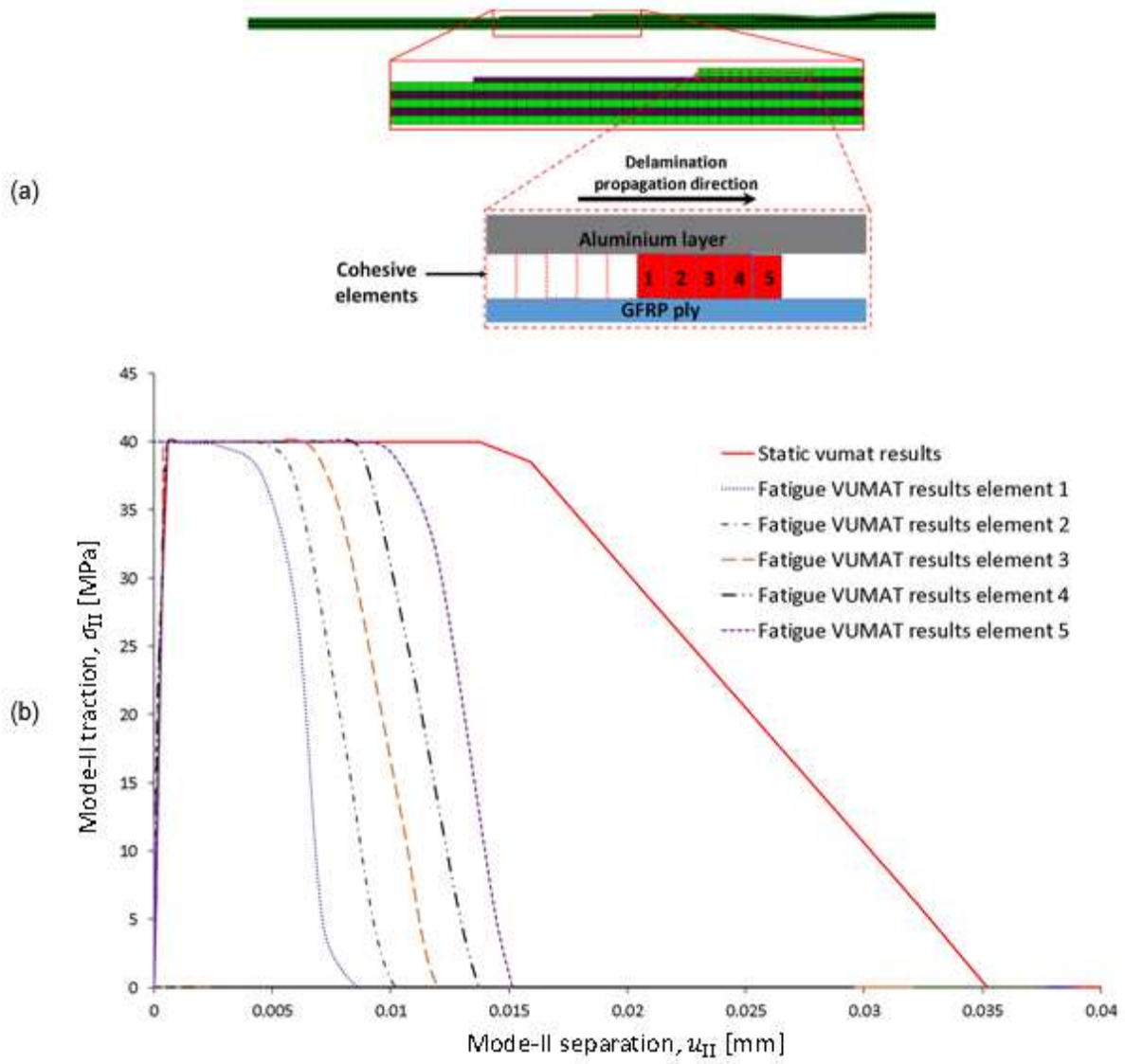

Figure 16: (a) Location of four cohesive elements in the splice model selected (arbitrarily) for detailed data output, and (b) comparison between static and fatigue traction-separation curves (50% severity) for these elements.

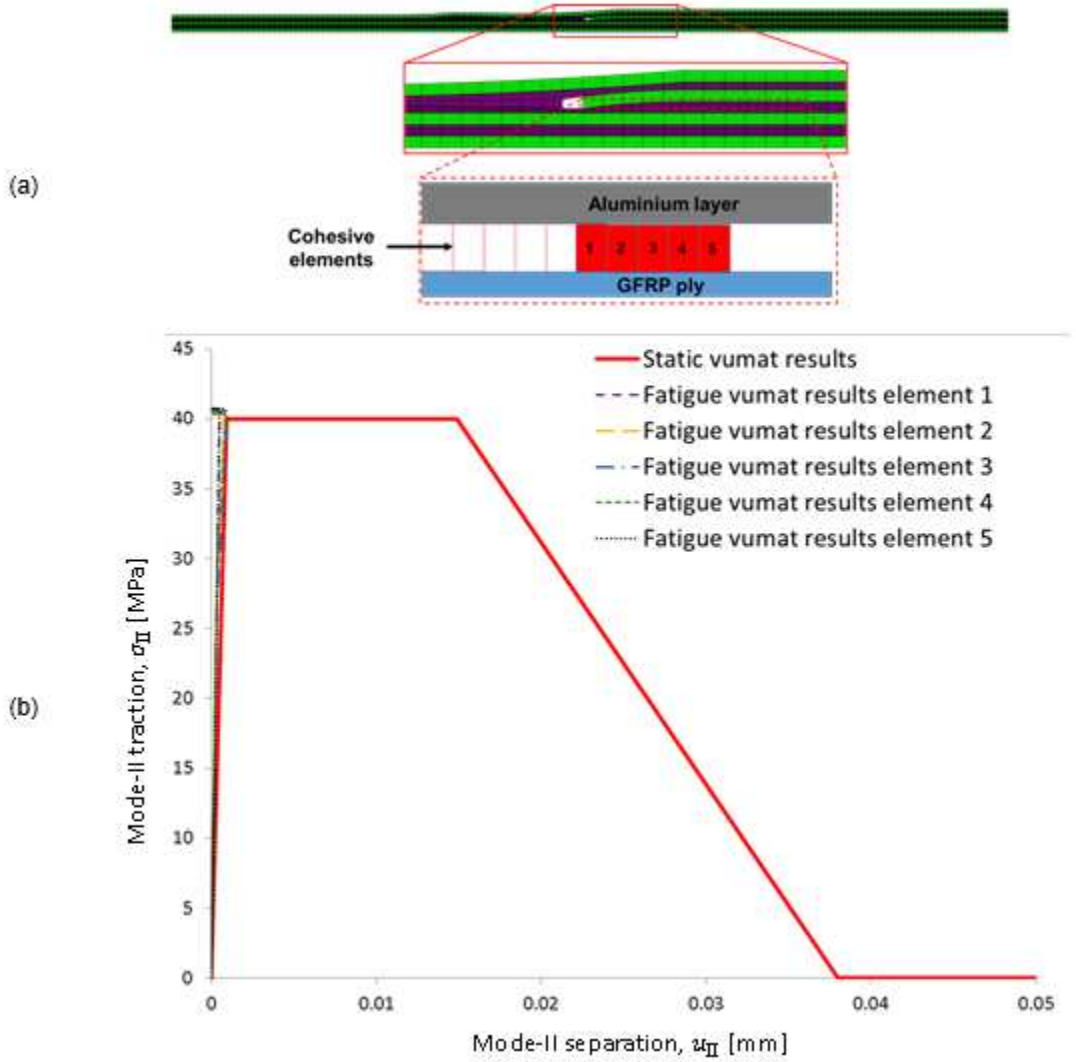

Figure 17: (a) Location of four cohesive elements in the doubler model selected (arbitrarily) for detailed data output, and (b) comparison between static and fatigue traction-separation curves (50% severity) for these elements.

For the doubler model, traction–separation curves are shown in Figure 17 for a series of five cohesive elements 5 mm from the crack tip in the path of the fatigue crack propagation. As for the splice specimens, these elements were chosen to validate the VUMAT code since at this stage the crack growth is stable. The upper and lower interfaces behave in exactly the same way, so only the results for the lower interface are shown. The fatigue traction-separation curves follow the reference (static) curve up to the end of elastic region, at a displacement of 0.82 µm. However, unlike the splice, after this point no fatigue degradation occurs in any of the elements along the interface indicating that delamination does not propagate along either the upper or the lower interfaces. This is consistent with the experimentally derived S-N curves discussed next.

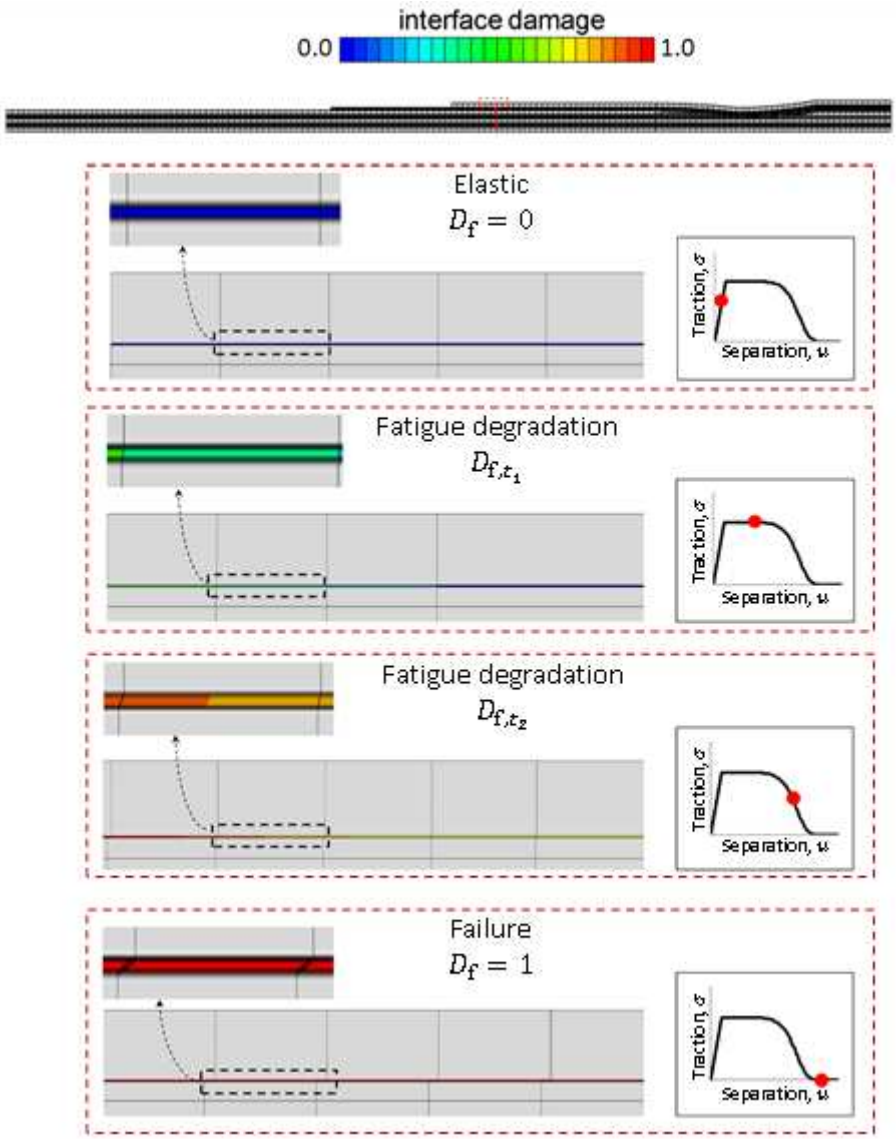

Figure 18: Contour plots of the damage variable D_f for cohesive elements in the splice specimen under fatigue loading (50% severity) showing the progressive nature of fatigue damage accumulation.

5 Experimental results

Fatigue test data for the splice and doubler specimens (pristine and pre-cracked) are presented in Table 7. Pairs of points taken from tests at different severities are used to plot S-N curves for both types of specimens in Figure 20 (solid lines represent trend lines). The S-N curves show the expected relationship between stress and average cycles to failure for both the doubler and splice. The results reveal that the fatigue life for the doubler specimens is considerably higher than for the splice specimens, corresponding to the doubler joint exhibiting a higher fatigue damage tolerance compared with the splice joint. This is in agreement with the fact that delamination initiates and grows in the external discontinuous aluminium/GFRP interfaces for the splice specimens causing

significant stiffness degradation as shown in Figure 21, while the doubler specimens do not show any delamination. Final fatigue failure occurred in the outer aluminium layers in the thinner cross section for both splice and doubler specimens.

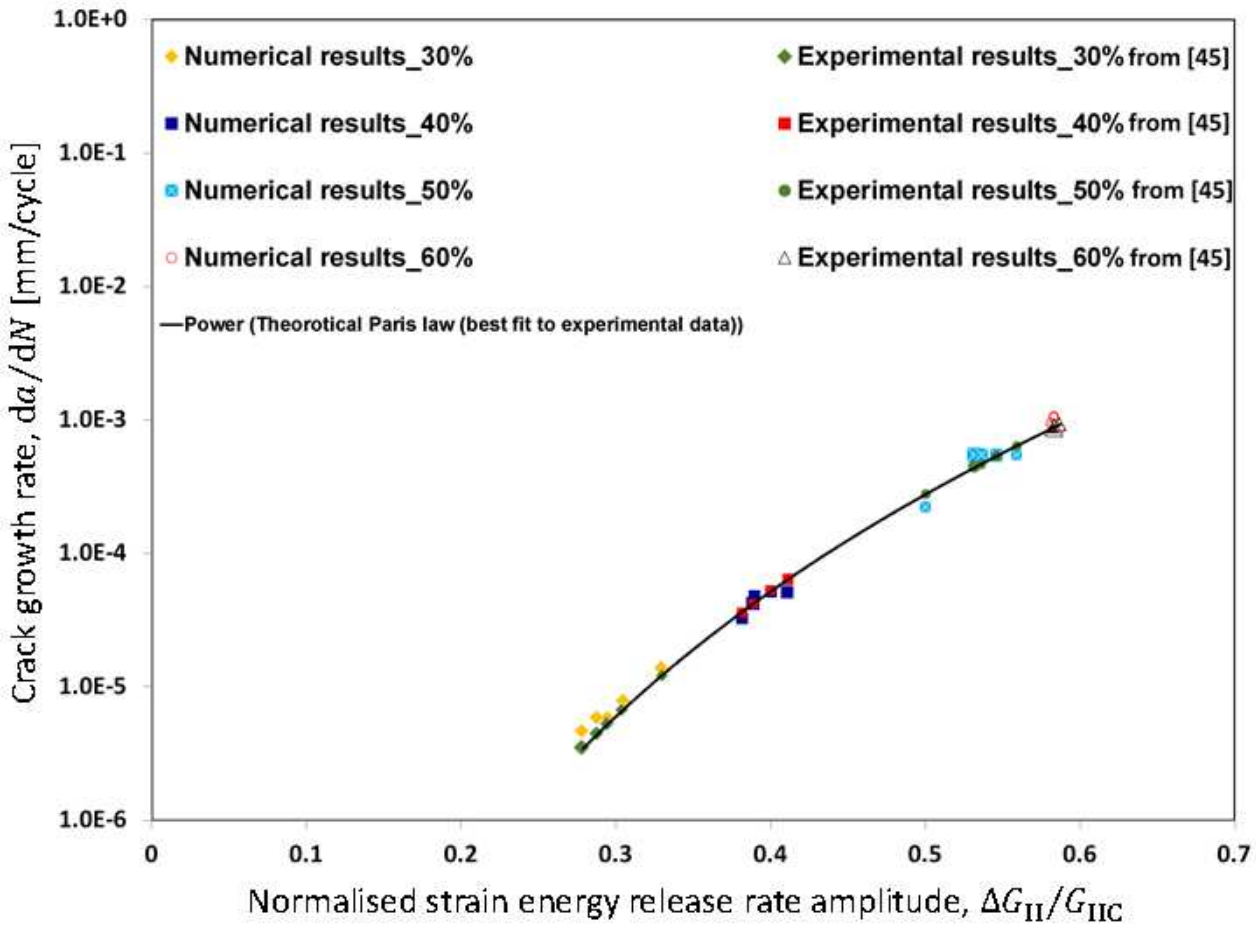

Figure 19: Experimental [45] and numerical Paris curves for the splice model under $R = 0.1$ and severities of 70%, 60%, 50% and 40%, as computed by the four output cohesive elements.

Table 7: Fatigue test results for the splice and doubler specimens.

Specimen	Peak load (kN)	Severity (%)	Fatigue life (cycles) Set-1	Fatigue life (cycles) Set-2
Splice	5.682	60	55912	49187
	4.735	50	110055	141878
	4.261	45	185093	180931
	3.788	40	374187	551276
	3.314	35	Run out	Run out
Pristine doubler	6.260	50	35156	48874
	5.008	40	161388	201607
	4.382	35	456228	424827
	3.756	30	896389	769385
	3.130	25	Run out	Run out

	6.260	50	49547	55945
Pre-cracked	5.008	40	169251	174165
doubler	4.382	35	394311	455357
	3.756	30	904207	912823
	3.130	25	Run out	Run out

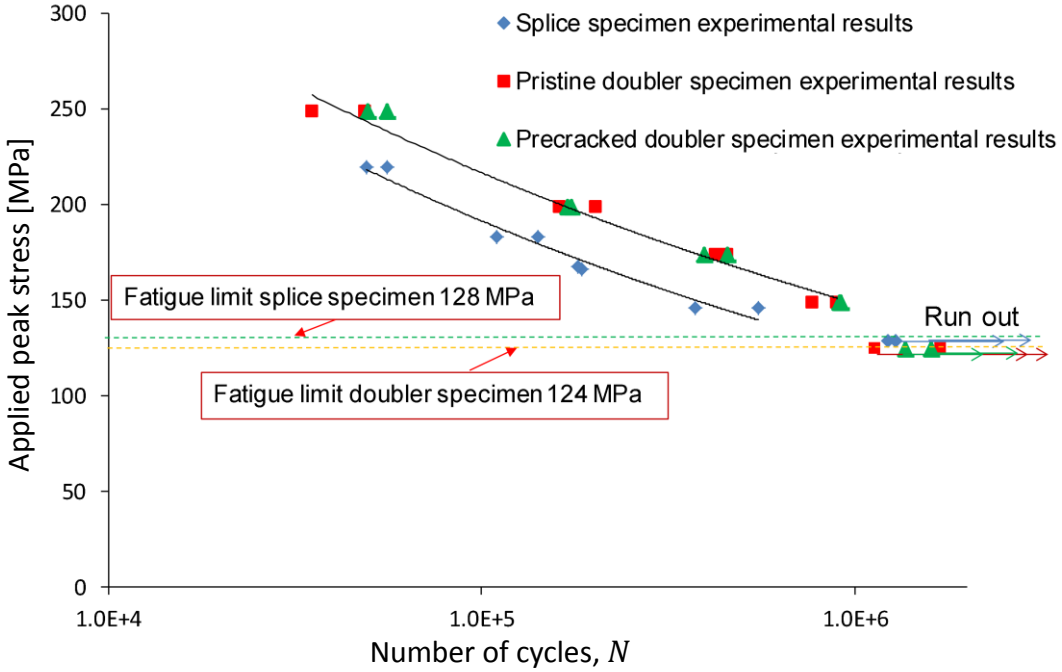

Figure 20: Experimental S-N curves for the splice and doubler specimens with R-ratio 0.1.

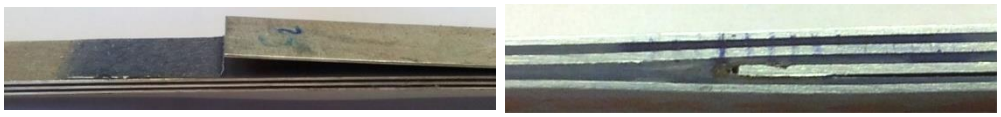

(a) (b)

Figure 21: Glare® 4B specimens after fatigue test with R-ratio 0.1 and maximum severities of (a) 60% for splice and (b) 50% for doubler specimens.

Further insight into the initiation and propagation of damage is provided by the AE results. Figures 22 and 23 show cumulative AE energy and AE amplitude against time, respectively, for splice specimens. During the first 1,300 seconds of the test (Figure 22 region A) the axial displacement increases from 0 to 0.3 mm, cumulative energy remains very low and AE signals are detected with amplitudes in the range of about 45-65 dB (Figure 23 region 1). This is potentially due to plastic deformation in the aluminium layers as observed in [53, 54], in which it was observed that plastic deformation in metals was accompanied by pronounced AE activity with an amplitude dependent on the type of metal. During the time period 1,300-4,000 s (Figure 22 region B) cumulative energy starts to increase gradually, potentially due to matrix cracking as demonstrated by [55, 56], resulting in AE

signals with an amplitude range of about 45-75 dB (Figure 23 region 2). This is accompanied by a small jump in axial displacement as seen in Figure 22.

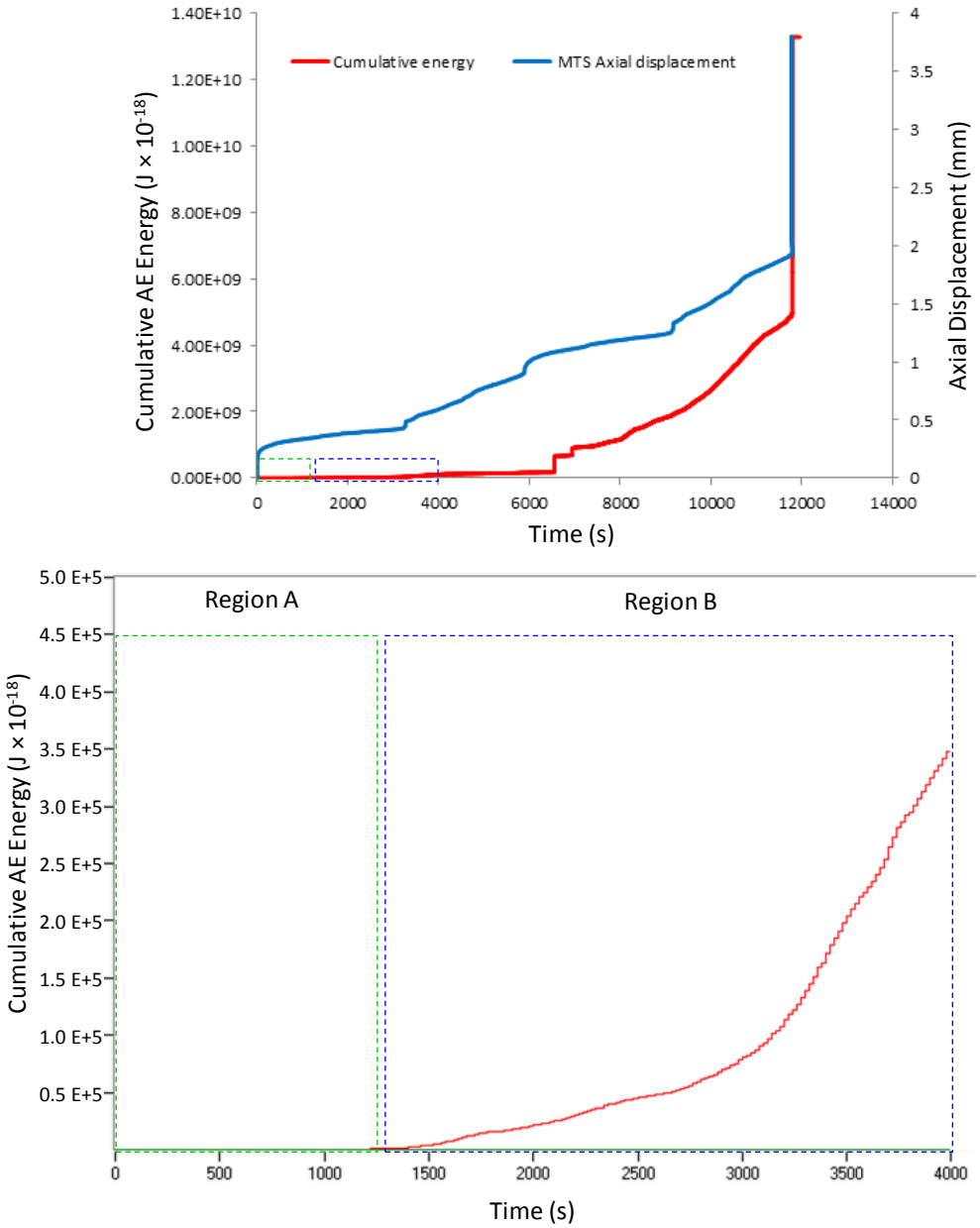

Figure 22: (a) Comparison between cumulative AE energy and axial displacement versus time for splice specimen under fatigue load with severity 60% and R-ratio of 0.1; (b) detailed curve of cumulative AE energy versus time for $0 < t < 4{,}000$ s.

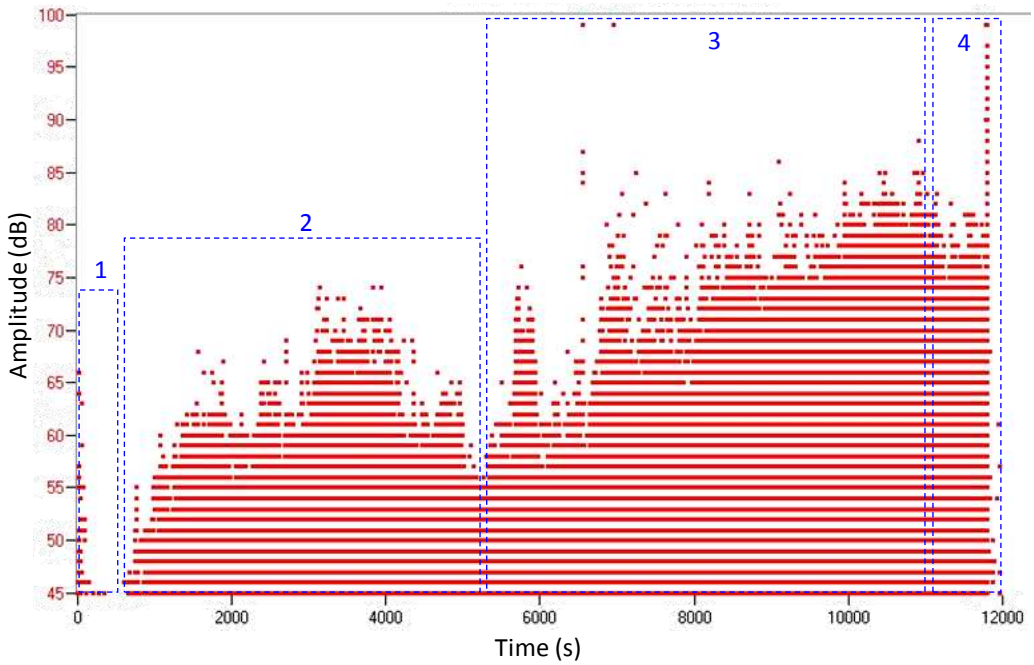

Figure 23: Amplitude-versus time for splice specimen under fatigue load with severity 60% and R-ratio 0.1.

Delamination initiation and growth are observed in the experiments during the period 5,500-11,000 s, and are seen to correspond to a gradual increase in the amplitude of the AE events which rise to a range of about 75-98 dB (Figure 23 region 3). This is accompanied by a steady increase in energy followed by a jump at a time of about 6,500 s. Finally, a small number of high amplitude events are seen in the range 87-98 dB (Figure 23 region 4) accompanied by a gradual increase followed by a large jump in cumulative energy and axial displacement during time period 11,000-12,000 s, observed to correspond to crack initiation and growth in the aluminium layers of the thinner region of the specimen followed by complete failure of the aluminium and hence the specimen.

For the doubler specimens, AE results show similar behaviour for both pristine and pre-cracked specimens with the results for pristine specimen being presented in Figures 24 and 25. As for the splice specimens, high amplitude events were recorded at the beginning of the test with an amplitude range of 45-77 dB (Figure 25 region 1) while cumulative energy remained constant up to 500 s (Figure 24, region A). This was accompanied by an increase in axial displacement to about 0.5 mm, which again is anticipated to be mostly due to plastic deformation in the aluminium layers. During the time period from 550-4,000 s, AE activity increases as the test progresses (Figure 24 - region B) alongside an increase in axial displacement up to about 6 mm at time 5,500 s. This is accompanied by a gradual increase in the amplitude of the signals to between 45-87 dB (Figure 25 region 2) believed to be caused by matrix cracking in the doubler joint [55, 56]. This is followed during the time

period 5,500-6,500 s, by fibre breakage in the discontinuous GFRP layers, characterised by signal amplitudes of between 45-98 dB (Figure 25 region 3) again in agreement with reports in the literature [55, 56], accompanied by a large jump in cumulative energy and a noticeable increase in axial displacement as shown in Figure 24. Finally, a steady increase in signals in the amplitude range of 87-98 dB is noticed (Figure 25 region 3), accompanied by a large jump in cumulative energy and axial displacement, corresponding to the propagation of cracks and then failure of the aluminium layers in the thinner section of the specimens, as observed during the test and confirmed by visual inspection of the failed specimens.

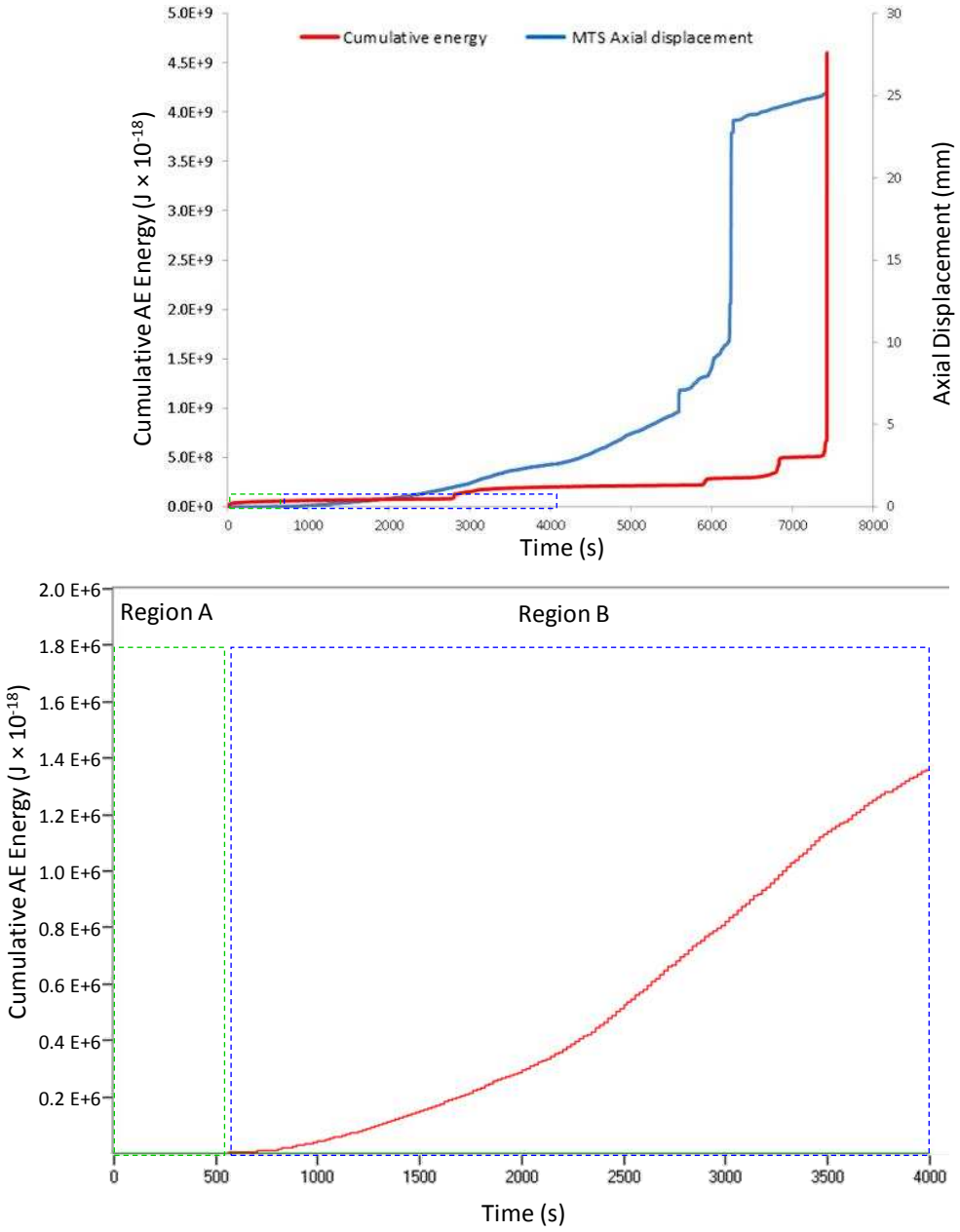

Figure 24: (a) Comparison between cumulative AE energy and axial displacement versus time for a doubler specimen under fatigue load with severity 50% and R-ratio of 0.1; (b) detailed curve of cumulative AE energy versus time for $0 < t < 4{,}000$ s.

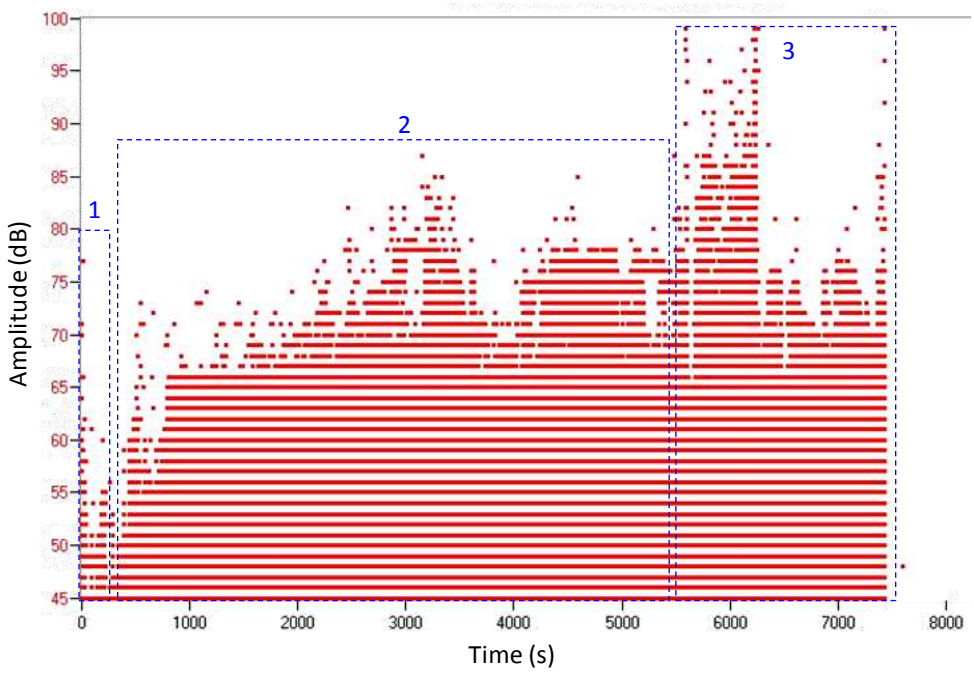

Figure 25: Amplitude-versus time for pristine doubler specimen under fatigue load with severity 50% and R-ratio 0.1.

6 Conclusions

A novel cohesive zone model incorporating a mixed-mode trapezoidal traction-separation law was developed to simulate delamination initiation and growth in FML specimens including splice and doubler features, under both static and high-cycle fatigue loading. A series of experiments were performed on both types of specimen under constant amplitude high-cycle fatigue loading for validation. The experimental results showed that the fatigue life for doubler specimens was higher than for splice specimens as the doubler joint exhibited high fatigue damage tolerance compared with the splice joint. Pristine and pre-cracked doubler specimens did not show any delamination under fatigue loading while in the splice specimens delaminations occurred in the discontinuous outer aluminium layer / GFRP ply interfaces. Good correlation was observed between the FE results and the experiments for both splice and doubler specimens in terms of delamination propagation using the Paris law. These results revealed that CZM based on trapezoidal traction-separation enables the prediction of delamination growth in ductile adhesives more efficiently than bilinear CZM making it more suitable for modelling interfacial damage initiation and growth for any adhesive with plastic flow properties. AE results were successfully used to validate numerical fatigue results in terms of delamination initiation and propagation detection via high cumulative energy events.

7 Acknowledgements

The authors would like to thank Iraqi Ministry of higher education and scientific research for supporting this research and the technical staff of School of Engineering, Cardiff University for their kind assistance with manufacturing specimens and the testing programme.

8 References

[1] A. Vlot and J.W. Gunnink, Fibre Metal Laminates - An Introduction. London: Kluwer Academic publishers, 2001.

[2] D.S. Dugdale, Yielding of Steel Sheets Containing Slits, J Mech Phys Solids, 8 (1960), pp. 100-104.

[3] A. Turon, J. Costa, P.P. Camanho, C.G. Dávila, Simulation of delamination in composites under high-cycle fatigue, Compos A, 38 (2007), pp. 2270–2282.

[4] M.F.S.F. de Moura and J.P.M. Gonçalves, Cohesive zone model for high-cycle fatigue of composite bonded joints under mixed-mode I+II loading, Eng Frac Mech, 140 (2015), pp. 31–42.

[5] P. Robinson, U. Galvanetto, D.Tumino, G. Bellucci and D. Violeau, Numerical simulation of fatigue-driven delamination using interface elements, Int J Numer Methods Eng, 63 (2005), pp. 1824–1848.

[6] P.W. Harper and S.R. Hallett, A fatigue degradation law for cohesive interface elements – Development and application to composite materials, Int J Fatigue, 32 (2010), pp. 1774–1787.

[7] L.F. Kawashita and S.R. Hallett, A crack tip tracking algorithm for cohesive interface element analysis of fatigue delamination propagation in composite materials, Int J Solids Struct, 49 (2012), pp. 2898–2913.

[8] W.H. Dennis, Metallurgy: 1863-1963. USA: Library of Congress Catalog 2010.

[9] M.M.A. Wahab, I.A. Ashcroft, A.D. Crocombe and S.J. Shaw, Prediction of fatigue thresholds in adhesively bonded joints using damage mechanics and fracture mechanics, J Adhes Sci Technol, 15 (2001), pp. 763-781.

[10] M. Imanaka, T. Hamano, A. Morimoto, R. Ashino and M. Kimoto, Fatigue damage evaluation of adhesively bonded butt joints with a rubber-modified epoxy adhesive, J Adhes Sci Technol, 17 (2003), pp. 981-994.

[11] I. Hilmy, M.M.A. Wahab, I.A. Ashcroft and A.D. Crocombe, Measuring of damage parameters in adhesive bonding, Key Eng Mat, 324-325 (2006), pp. 275-278.

[12] I. Hilmy, M.M.A. Wahab, A.D. Crocombe, I.A. Ashcroft and A.G. Solana, Effect of triaxiality on damage parameters in adhesive, Key Eng Mat, 348-349 (2007), pp. 37-40.

[13] G. Barenblatt, The Mathematical Theory of Equilibrium Cracks in Brittle Fracture, Adv in Appl Mech, 7 (1962), pp. 55-129.

[14] A. Hillerborg, M. Modeer and P-E. Petersson, Analysis of crack formation and crack growth in concrete by means of fracture mechanics and finite elements, Cem Concr Res, 6 (1976), pp. 773–81.

[15] A. Needleman, A continuum model for void nucleation by inclusion debonding, J Appl Mech, 54 (1987), pp. 525–531.

[16] V. Tvergaard and J.W. Hutchinson, The relation between crack growth resistance and fracture process parameters in elastic-plastic solids, J. Mech. Phys. Solids, 40 (1992), pp. 1377-1397.

[17] S. Maiti and P.H. Geubelle, A cohesive model for fatigue failure of polymers, Eng Fract Mech, 72 (2005), pp. 691–708.

[18] O. Nguyen, E. Repetto, M. Ortiz, and R. Radovitzky, A cohesive model of fatigue crack growth, Int J Fract, 4 (2001), pp. 351–369.

[19] T. Siegmund, A numerical study of transient fatigue crack growth by use of an irreversible cohesive zone model, Int J Fatigue, 26 (2004), pp. 929–939.

[20] Y.J. Xu and H. Yuan, Computational analysis of mixed-mode fatigue crack growth in quasi-brittle materials using extended finite element methods, Eng Fract Mech, 76 (2009), pp. 165–81.

[21] K.L. Roe and T. Siegmund, An irreversible cohesive zone model for interface fatigue crack growth simulation, Engineering Fract Mech, 70 (2003), pp. 209-232.

[22] A. Ural and K. Papoulia, Modeling of fatigue crack growth with a damage-based cohesive zone model, presented at the 4th European Congress on Computational Methods in Applied Sciences and Engineering, Finland, 2004.

[23] S.R. Hallett and M. May, A combined model for initiation and propagation of damage under fatigue loading for cohesive interface elements, Compos A, 41 (2010), pp. 1787–1796.

[24] H. Khoramishad, A.D. Crocombe, K.B. Katnam and I. A. Ashcroft, Predicting fatigue damage in adhesively bonded joints using a cohesive zone model, Int J Fatigue, 32 (2010), pp. 1146–1158.

[25] S. Sugiman and A.D. Crocombe, The static and fatigue response of metal laminate and hybrid fibre-metal laminate doublers joints under tension loading, Compos Struct, 94 (2012), pp. 2937–2951.

[26] F. Mazaheri and H. Hosseini-Toudeshky, Low-cycle fatigue delamination initiation and propagation in fibre metal laminates, Fatigue Fract Engng Mater Struct, 38 (2015), pp. 641–660.

[27] R.D.S.G. Campilho, M.D. Banea, J.A.B.P. Neto and L.F.M. da Silva, Modelling adhesive joints with cohesive zone models: effect of the cohesive law shape of the adhesive layer, Int J Adhes Adhes, 44 (2013), pp. 48–56.

[28] G. Alfano and M.A. Crisfield, Finite element interface models for the delamination analysis of laminated composites: mechanical and computational issues, Int J for Numer Methods Eng, 7 (2001), pp. 1701–1736.

[29] O. Nguyen, E. Repetto, M. Ortiz and R. Radovitzky, A cohesive model of fatigue crack growth, Int J Fract, 4 (2001), pp. 351–369.

[30] B.F. Sørensen, Cohesive law and notch sensitivity of adhesive joints, Acta Materialia, 5 (2002), pp. 1053–1061.

[31] D. Xie and J.S.B. Biggers, Progressive crack growth analysis using interface element based on the virtual crack closure technique, Finite Elem Anal Des, 11 (2006), pp. 977–984.

[32] D. Xie and A.M. Waas, Discrete cohesive zone model for mixed-mode fracture using finite element analysis, Eng Fract Mech, 13 (2006), pp. 1783– 1796.

[33] P.A. Gustafson and A.M. Waas, T650/AFR-PE-4/FM680-1 mode I critical energy release rate at high temperatures: experiments and numerical models, presented at the AIAA/ASME/ASCE/AHS/ASC 48th Structures, Structural Dynamics, and Materials Conference, Honolulu, 2007.

[34] C. Sun, Fracture of plastically deforming adhesively bonded structures: experimental and numerical studies, PhD thesis, University of Michigan, 2007.

[35] P.A. Gustafson and A.M. Waas, The influence of adhesive constitutive parameters in cohesive zone finite element models of adhesively bonded joints, Int J Solids Struct, 46 (2009), pp. 2201–2215.

[36] J.C. Brewer, P.A. Lagace, Quadratic stress criterion for initiation of delamination, Journal of composite materials 22 (1988), pp.1141-1155.

[37] Wen-Guang Jiang, S.R. Hallett, B.G. Green and M.R. Wisnom, A concise interface constitutive law for analysis of delamination and splitting in composite materials and its application to scaled notched tensile specimens, Int J Numer Methods Eng, 69 (2007), pp. 1982-1995.

[38] V. Rooijen, Bearing Strength Characteristics of Standard and Steel Reinforced GLARE®, PhD thesis, Delft University of Technology, 2006.

[39] M. Vesco and J. Sinke, Response and Damage Evolution in Glare® Laminates under Indentation Loads - Experimental Results, Delft University of Technology 2005.

[40] Ahmad S.M. Al-Azzawi, L.F. Kawashita and C.A. Featherston, Buckling and Postbuckling Behaviour of Glare® Laminates Containing Splices and Doublers. Part 2: Numerical Modelling, Compos Struct, 176 (2017), pp. 1170–87.

[41] Ahmad S.M. Al-Azzawi, M.S. Al-Saymaree, L.F. Kawashita and C.A. Featherston, Quasi-static Damage in Fibre Metal Laminate Adhesive Joints: Experimental Investigations, accepted for presentation at 20th International Conference on Composite Structures (ICCS-20), Paris, France, 4-7 September 2017.

[42] Ahmad S.M. Al-Azzawi, L.F. Kawashita and C.A. Featherston, Delamination Characteristics of Glare® Laminates Containing Doubler and Splice Features Under High Cycle Fatigue Loading, presented at the the 24th UK Conference of the Association for Computational Mechanics in Engineering, Cardiff University, Cardiff, UK, 2016.

[43] A. Amiri-Rad, M. Mashayekhi, F.P. Van der Meer and H. Hadavinia, A two-scale damage model for high cycle fatigue delamination in laminated composites, Compos Sci Technol, 120 (2015), pp. 32-38.

[44] Dassault Systèmes Simula Corp., Abaqus User's Manual, version 6.12, 2012.

[45] R.C. Alderliesten, Fatigue Crack Propagation and Delamination Growth in Glare®, PhD thesis, Delft University of Technology, 2005.

[46] P. Naghipour, K. Schulze, J. Hausmann and M. Bartsch, Numerical and experimental investigation on lap shear fracture of Al/CFRP laminates, Compos Sci Technol 72 (2012), pp. 1718–1724.

[47] L. Kawashita, A. Kinloch, D. Moore and J. Williams, The influence of bond line thickness and

peel arm thickness on adhesive fracture toughness of rubber toughened epoxy aluminium alloy laminates, Inl J Adhes Adhes, 28 (2008), pp. 199-210.

[48] K.B. Katnam, A.D. Crocombe, H. Sugiman, H. Khoramishad and I.A. Ashcroft, Static and fatigue failures of adhesively bonded laminate joints in moist environments, Inl J Damage Mech, 20, 2011.

[49] A. Seyed-Yaghoubi and B. Liaw, Experimental and numerical approaches on behavior of Glare® 5 beams: Influences of thickness and stacking sequence, in Topics in Modal Analysis II, Volume 6: Proceedings of the 30th IMAC, J. D. C. in: R. Allemang, C. Niezrecki, J. Blough (Eds.), Ed., ed Springer New York, pp. 7-16, 2012.

[50] Cytec Engineering Materials, FM® 94 Adhesive Film Technical Data Sheet, Ed., 2010.

[51] M. Hagenbeek, Characterisation of Fibre Metal Laminates under Thermo-mechanical Loadings, PhD thesis, Delft University of Technology, 2005.

[52] Ahmad S.M. Al-Azzawi, L.F. Kawashita, and C.A. Featherston, Modelling Fatigue Damage in Fibre Metal Laminate Adhesive Joints, accepted for presentation at 21st International Conference on composite Materials (ICCM-21), in Xi'an, China, 20-25 August 2017.

[53] J. Miloš, K. Robert, D. Patrik, C. František, Š. Vladimír and F. Holländer, Mechanisms of plastic deformation in AZ31 magnesium alloy investigated by acoustic emission and transmission electron microscopy, Mater Sci Eng: A, 462 (2007), pp. 311-315.

[54] A. Vinogradov, D. Orlov, A. Danyuk and Y. Estrin, Effect of grain size on the mechanisms of plastic deformation in wrought Mg-Zn-Zr alloy revealed by acoustic emission measurements, Acta Materialia, 61 (2013), pp. 2044-2056.

[55] P.F. Liu, J.K. Chu, Y.L. Liu and J.Y. Zheng, A study on the failure mechanisms of carbon fiber/epoxy composite laminates using acoustic emission, Mater Des, 37 (2012), pp. 228-235.

[56] X. Zhuang and X. Yan, Investigation of Damage Mechanisms in Self-Reinforced Polyethylene Composites by Acoustic Emission, Compos Sci Tech, 66 (2006), pp. 444-449.